

SOLAR ACTIVE REGION AND QUIET-SUN EXTREME-ULTRAVIOLET SPECTRA FROM SERTS-95

JEFFREY W. BROSIUS,¹ JOSEPH M. DAVILA, AND ROGER J. THOMAS

Code 682, NASA/Goddard Space Flight Center, Greenbelt, MD 20771

Received 1998 April 28; accepted 1998 July 13

ABSTRACT

Goddard Space Flight Center's Solar EUV Rocket Telescope and Spectrograph was flown on 1995 May 15 (SERTS-95), carrying a multilayer-coated toroidal diffraction grating that enhanced the instrumental sensitivity in its second-order wave band (171–225 Å). Spectra and spectroheliograms of NOAA active region 7870 (N09 W22) were obtained in this wave band with a spectral resolution (instrumental FWHM) ~ 30 mÅ and in the first-order wave band (235–335 Å) with a spectral resolution ~ 55 mÅ. Spectra and spectroheliograms of quiet-Sun areas northeast of the active region were also obtained. We derived the SERTS-95 relative radiometric calibration directly from flight data by means of density- and temperature-insensitive line intensity ratios. Most theoretical values for such ratios were obtained from the CHIANTI database. A total of 44 different lines were used to derive the relative radiometric calibration in the two spectral orders, most of them coming from seven (Fe x–Fe xvi) of the nine (Fe ix–Fe xvii) observed ionization stages of iron. The resulting relatively calibrated line intensities agree well with their corresponding normalized theoretical values. This supports the overall accuracy of the atomic physics parameters and demonstrates the power of the technique. The present work extends earlier work by Brosius, Davila, & Thomas, who determined the SERTS-95 second-order response using this technique. Many of the ratios employed here can be used to carry out a similar calibration exercise on spectra from the Coronal Diagnostic Spectrometer (CDS) aboard the *Solar and Heliospheric Observatory* (SOHO). We placed the line intensities onto an absolute scale by forcing our quiet-Sun He ii $\lambda 303.8$ + Si xi $\lambda 303.3$ intensity to match that from previous observations. The resulting active region and quiet-Sun absolutely calibrated line lists contain 127 and 20 lines, respectively. Active region densities derived from density-sensitive line intensity ratios of Fe x, xi, xiii, and xiv are mutually consistent with $\log n_e \sim 9.4 \pm 0.2$; densities derived from Fe xii are significantly greater ($\log n_e \sim 10$).

Subject headings: instrumentation: spectrographs — Sun: activity — Sun: corona — Sun: UV radiation

1. INTRODUCTION

Reliable measurements of the density, filling factor, emission measure, and magnetic field strength are essential for understanding the multithermal structures found in the solar corona and for determining the physical processes that occur in those structures. The extreme-ultraviolet (EUV) wave band (150–1200 Å) contains emission lines formed at temperatures ranging from several 10^4 K to several 10^7 K and is therefore well suited for studies of those multithermal coronal structures. This is why the EUV wave band was chosen for Goddard Space Flight Center's Solar EUV Rocket Telescope and Spectrograph (SERTS), as well as for the Coronal Diagnostic Spectrometer (CDS) aboard the NASA/ESA *Solar and Heliospheric Observatory* (SOHO) spacecraft.

Malinovsky & Heroux (1973) obtained solar spectra between 50 and 300 Å with a spectral resolution (FWHM of the instrumental line shape) ~ 250 mÅ during a sounding rocket flight. The estimated accuracy of their absolute intensities varies from 20% to 50% depending upon the ratio of the line intensity to background; however, no corrections for atmospheric absorption were applied. Further, the Malinovsky & Heroux (1973) spectrum was acquired from full-Sun observations and so provides no information about distinct solar features.

Vernazza & Reeves (1978) obtained spatially resolved ($5'' \times 5''$) spectra between 280 and 1350 Å with a spectral

resolution ~ 1.6 Å using the Harvard EUV spectrometer-spectroheliometer on *Skylab*. They present composite spectra of different solar features obtained during 9 months of observation near solar minimum (1973 May–1974 February). Although their intensity uncertainty approaches a factor of 2 for wavelengths toward the lower end of their wave band, their average quiet-Sun He ii $\lambda 304$ intensity is comparable to our value reported in Table 1.

Doschek & Cowan (1984) present a semiempirical “emission rate spectrum” between 10 and 200 Å, based upon a composite of observed solar quiet-Sun and flare spectra supplemented with theoretical calculations. This spectrum represents that emitted by a plasma with solar photospheric abundances and a constant emission measure distribution between 2.5×10^5 and 2.0×10^7 K. Nearly 40% of their lines are not observed in actual solar spectra because of instrumental sensitivity limitations or because the Sun has relatively little plasma at the lines' formation temperature ($\sim 10^5$ K). The latter is probably why the oxygen and neon lines listed by Doschek & Cowan (1984) are not seen in SERTS active region spectra.

Behring et al. (1976) obtained solar EUV spectra with 60 mÅ spectral resolution during two sounding rocket flights and provided many line identifications. However, those spectra were acquired from full-Sun observations and so provide no information about distinct solar features. Furthermore, the relative line intensities were only approximately calibrated, which renders line intensity ratio measurements uncertain. Observations obtained with the NRL slitless spectrograph on *Skylab* (Tousey et al. 1977) provided high spatial ($2''$) and spectral (~ 100 mÅ)

¹ Raytheon STX Corporation, 4400 Forbes Boulevard, Lanham, MD 20706.

TABLE 1
SERTS-95 ABSOLUTELY CALIBRATED QUIET-SUN LINE LIST DERIVED FROM
SPATIALLY AVERAGED SLIT SPECTRA

Ion	Wavelength	$I \pm \sigma_I$	FWHM $\pm \sigma_{fwhm}$
Fe IX	171.082	(392.0 ± 103.0)	32.6 ± 6.1
Fe X	174.534	556.0 ± 110.0	48.8 ± 6.5
Fe X	177.246	253.0 ± 67.0	37.5 ± 7.0
Fe XI	180.405	528.0 ± 76.6	43.0 ± 4.2
.....	180.466	184.0 ± 99.1	40.8 ± 20.1
Fe XI	182.157	121.0 ± 24.2	32.5 ± 4.4
Fe X	184.548	182.0 ± 43.5	55.4 ± 9.4
Fe XII	186.885	73.9 ± 27.3	29.0 ± 7.9
Fe VIII	187.250	50.5 ± 20.7	29.4 ± 8.9
Fe XI	188.218	200.0 ± 46.0	39.3 ± 6.3
(Fe XI)	188.303	138.0 ± 34.2	39.1 ± 6.8
Fe XII	192.385	99.2 ± 22.1	88.8 ± 13.7
Fe XI	192.827	53.0 ± 14.1	60.1 ± 11.3
Fe XII	193.512	196.0 ± 28.3	63.2 ± 5.4
Fe XII	195.128	312.0 ± 38.8	46.0 ± 3.0
S VII + Fe XI	198.521	91.6 ± 21.7	39.1 ± 6.4
(Fe XII, Fe XI)	201.733	118.0 ± 23.1	26.6 ± 3.5
Fe XIII	202.056	253.0 ± 40.6	34.1 ± 3.4
Fe XIII	203.836	92.6 ± 32.3	36.0 ± 9.2
He II	303.782	9510.0 ± 1070.0	111.0 ± 5.7

NOTE.—Intensities are in $\text{ergs cm}^{-2} \text{s}^{-1} \text{sr}^{-1}$

resolution images in the 171–630 Å wave band but were limited by the overlap of images from nearby spectral lines. They provided excellent diagnostic capabilities for small, intense sources such as flares (see, e.g., Dere 1978; Dere et al. 1979) but were less well suited for quiet-Sun areas and quiescent active regions.

SERTS was designed to improve upon earlier solar EUV instrumentation by (1) retaining the stigmatic imaging capability of the NRL spectroheliograph on *Skylab* while providing a spatial selection capability that reduces image overlap and (2) achieving high spectral resolution ($\sim 55/N$ mÅ, where N is the spectral order). The configuration of the SERTS entrance aperture enables both spectra and spectroheliograms to be obtained simultaneously: spectra are obtained along a narrow 5' long slit connecting two rectangular lobes within which the spectroheliograms are imaged. Because the lobes cover areas of approximately $5' \times 8'$ on the Sun, the amount of image overlap is less than one-sixth that of the *Skylab* spectroheliograph. The spatial resolution is $\sim 5''$. By adjusting the pointing of the instrument during its flight, both images and spectra are obtained for the same areas on the Sun.

The version of SERTS flown in 1989 (SERTS-89) (Neupert et al. 1992; Thomas & Neupert 1994; Young, Landi, & Thomas 1998) carried a standard gold-coated toroidal diffraction grating. It observed hundreds of first-order emission lines between 235 and 450 Å, as well as dozens of second-order lines between 170 and 225 Å. The version of SERTS flown in 1991 (SERTS-91) (Davila et al. 1993; Brosius et al. 1993, 1996a, 1996b) and 1993 (SERTS-93) (Brosius et al. 1996a, 1996b, 1997a, 1997b) carried a multilayer-coated diffraction grating that enhanced the instrumental efficiency in the first-order wavelength range, while the version flown in 1995 (SERTS-95) (Brosius, Davila, & Thomas 1998) incorporated a multilayer grating that enhanced the instrumental sensitivity in the second-order wave band (~ 170 –225 Å). This enhancement brings out many lines that were not seen during any of the previous flights, which allows them to be measured with the highest spectral resolution ever achieved for spatially

resolved active region and quiet-Sun spectra in this wavelength range (~ 30 mÅ). Furthermore, the multilayer grating used for the 1995 flight also permitted the detection of numerous first-order lines between 235 and 340 Å and a few lines at wavelengths up to 450 Å. In this paper we present absolutely calibrated SERTS-95 active region and quiet-Sun spectral line catalogs covering the 171–340 Å wavelength range. These data combine, for the first time, both high spectral resolution and reliable radiometric calibration in this range.

Section 2 describes the SERTS-95 observations; § 3 explains the relative and absolute radiometric calibration technique; § 4 presents the active region emission line catalog; § 5 presents the quiet-Sun emission line catalog.

2. OBSERVATIONS

SERTS was launched on a Terrier-boosted Black Brant rocket from White Sands, NM, at 1800 UT on 1995 May 15. It reached a maximum altitude of 307 km and recorded spectrographic data on photographic film for nearly 7 minutes. This was the last flight for which data were recorded on film: subsequent flights utilized a CCD-intensified detector. The instrument performed well, obtaining four different exposures in each of two different pointing positions. This ensured the availability of optimally exposed spectral lines and spectroheliograms for both strong and weak spectral features and provided the information needed to determine the film's density versus log energy (D -log E) relation (see, e.g., Thompson et al. 1993). The wavelength scale was determined from laboratory measurements of He II and Ne II lines. Data were digitized with a Perkin-Elmer microdensitometer, and plate flaws were subsequently removed by replacing occasional defects with uncontaminated local pixel averages.

Spectroheliograms of NOAA active region 7870 (N09 W22) and slit spectra of quiet-Sun areas northeast of region 7870 were obtained in the first pointing position. We used the longest exposure in this position (99.4 s) to obtain the quiet-Sun spectrum given in Table 1. Slit spectra of region 7870 and spectroheliograms of quiet-Sun areas to the

TABLE 2
SERTS-95 ABSOLUTELY CALIBRATED ACTIVE REGION LINE LIST DERIVED FROM SPATIALLY AVERAGED SLIT SPECTRA

Ion	Wavelength	$I \pm \sigma_I$	FWHM $\pm \sigma_{\text{fwhm}}$
Fe ix	171.074	(208.0 \pm 62.0)	35.8 \pm 7.6
.....	172.335	84.9 \pm 35.5	24.7 \pm 7.6
Fe x	174.526	654.0 \pm 83.0	41.3 \pm 2.8
Fe x	175.265	135.0 \pm 32.4	27.2 \pm 4.6
.....	176.012	141.0 \pm 29.7	21.9 \pm 3.2
Fe x	177.240	335.0 \pm 47.5	38.6 \pm 3.2
.....	178.715	54.1 \pm 23.3	24.5 \pm 8.1
Ni xv + S ix	179.276	53.3 \pm 22.4	22.7 \pm 7.0
Fe xi + Fe xvi	180.382	3440.0 \pm 391.0	50.7 \pm 2.6
Fe xi	181.125	123.0 \pm 35.6	54.1 \pm 10.7
Fe xi	182.166	237.0 \pm 33.4	39.7 \pm 3.5
Fe x	184.534	164.0 \pm 23.8	33.3 \pm 2.9
Fe xi	184.800	31.5 \pm 14.0	28.7 \pm 9.5
.....	185.002	46.3 \pm 16.2	27.8 \pm 7.1
Fe viii + Ni xvi	185.221	305.0 \pm 42.3	70.2 \pm 5.6
Ca xiv	186.616	77.4 \pm 15.5	32.3 \pm 4.4
Fe xii	186.867	498.0 \pm 64.0	69.3 \pm 4.8
.....	186.968	22.8 \pm 4.1	26.3 \pm 3.1
Fe viii	187.247	15.6 \pm 7.4	18.2 \pm 6.9
Ar xiv	187.962	26.3 \pm 8.6	23.2 \pm 5.5
Fe xi	188.214	385.0 \pm 77.3	46.6 \pm 6.3
(Fe xi)	188.295	276.0 \pm 51.6	57.8 \pm 7.2
.....	188.494	35.7 \pm 8.4	26.0 \pm 4.2
S xi	188.663	56.4 \pm 14.0	44.6 \pm 7.8
Ar xi	188.821	28.3 \pm 10.7	25.4 \pm 7.0
.....	189.002	31.3 \pm 8.4	22.8 \pm 4.4
(Fe xi)	189.185	32.8 \pm 8.9	33.2 \pm 6.4
Fe xi	189.722	26.4 \pm 6.7	27.9 \pm 5.0
Fe x	190.046	47.9 \pm 9.4	42.1 \pm 5.5
S xi	191.257	42.6 \pm 9.7	55.2 \pm 8.8
Fe xii	192.390	206.0 \pm 25.1	51.2 \pm 3.2
Fe xi	192.813	68.3 \pm 9.8	43.1 \pm 4.1
Ca xvii	192.883	39.0 \pm 10.7	67.1 \pm 14.3
Fe xii	193.505	487.0 \pm 55.4	49.2 \pm 2.6
Ca xiv	193.872	76.2 \pm 10.7	58.0 \pm 4.7
Ni xvi	194.026	19.6 \pm 3.5	30.4 \pm 3.6
Ar xiv	194.401	18.5 \pm 6.8	20.7 \pm 5.6
Fe xii	195.117	869.0 \pm 100.0	49.3 \pm 2.7
Fe xiii	196.519	135.0 \pm 33.4	42.1 \pm 7.3
Fe xii	196.642	120.0 \pm 18.0	51.5 \pm 4.7
S viii + Fe xii	198.559	51.6 \pm 10.3	35.9 \pm 4.8
.....	198.845	56.9 \pm 16.9	61.2 \pm 13.2
Fe xiii	200.017	304.0 \pm 36.7	46.8 \pm 2.8
Ca xv	200.978	118.0 \pm 20.0	52.5 \pm 5.8
Fe xiii	201.118	470.0 \pm 60.6	48.8 \pm 3.4
(Fe xii, Fe xi)	201.759	75.2 \pm 19.3	59.4 \pm 10.8
Fe xiii	202.042	1210.0 \pm 138.0	49.6 \pm 2.6
Fe xiii	202.415	73.7 \pm 17.3	32.0 \pm 5.3
Fe xiii	203.164	154.0 \pm 24.2	36.8 \pm 3.6
.....	203.727	520.0 \pm 71.6	107.0 \pm 9.5
Fe xiii	203.820	1930.0 \pm 238.0	70.2 \pm 4.5
Fe xiii	204.255	195.0 \pm 29.7	48.0 \pm 4.5
Fe xvii	204.665	72.0 \pm 24.7	41.9 \pm 10.6
Fe xiii	204.950	267.0 \pm 44.5	63.7 \pm 6.7
K xvi	206.258	120.0 \pm 32.5	45.5 \pm 8.8
Si xi	207.660	56.6 \pm 18.4	26.4 \pm 6.2
.....	208.506	66.2 \pm 19.5	40.2 \pm 8.8
Fe xiii	209.623	210.0 \pm 33.1	44.4 \pm 4.4
Fe xiii	209.908	225.0 \pm 43.6	58.6 \pm 7.6
Fe xiv	211.317	2510.0 \pm 287.0	53.5 \pm 2.8
.....	211.431	138.0 \pm 23.8	55.6 \pm 6.6
Fe xii	211.736	94.2 \pm 29.1	35.7 \pm 7.9
S xii	212.088	78.6 \pm 16.7	41.8 \pm 6.1
.....	212.191	83.3 \pm 28.3	41.3 \pm 10.2
Fe xiii	213.764	91.7 \pm 20.6	34.2 \pm 5.3
Fe xii	214.400	68.3 \pm 27.6	35.2 \pm 11.3
Si viii	214.757	102.0 \pm 37.6	52.5 \pm 14.3
Si viii + Fe xiii	216.899	53.7 \pm 16.3	31.1 \pm 7.1
Fe xii	217.277	97.7 \pm 35.3	44.8 \pm 11.8
S xii	218.196	156.0 \pm 29.9	48.1 \pm 6.1
Fe ix	218.943	98.9 \pm 30.1	30.9 \pm 6.8
Fe xiv	219.121	748.0 \pm 89.1	48.5 \pm 2.9
Fe xii	219.449	73.5 \pm 22.5	46.3 \pm 10.6

TABLE 2—*Continued*

Ion	Wavelength	$I \pm \sigma_I$	FWHM $\pm \sigma_{\text{fwhm}}$
Fe xiv	220.090	621.0 \pm 84.2	69.9 \pm 5.4
Fe xblend	220.862	95.4 \pm 20.7	31.1 \pm 4.7
Fe xiii	221.813	218.0 \pm 32.5	30.1 \pm 2.7
Fe xi + Ca xvii	222.998	76.7 \pm 16.1	28.5 \pm 4.1
Ni xvi	239.504	156.0 \pm 61.0	50.6 \pm 15.2
.....	240.395	126.0 \pm 41.5	49.7 \pm 12.5
Fe xiii	240.687	160.0 \pm 66.2	71.9 \pm 21.7
.....	241.903	188.0 \pm 57.8	40.9 \pm 9.1
He ii	243.019	324.0 \pm 69.7	72.4 \pm 10.7
Fe xv	243.771	668.0 \pm 102.0	77.6 \pm 7.3
Fe xiii	246.187	246.0 \pm 47.4	68.7 \pm 8.9
S xi	247.143	151.0 \pm 53.3	76.9 \pm 20.8
Ni xvii	249.168	587.0 \pm 81.8	66.1 \pm 5.3
Fe xvi	251.053	521.0 \pm 74.6	71.3 \pm 6.0
Fe xiii	251.939	332.0 \pm 65.0	45.3 \pm 5.9
Fe xiv	252.168	364.0 \pm 73.3	99.6 \pm 13.6
.....	255.482	258.0 \pm 63.1	106.0 \pm 18.3
He ii + Si x	256.318	1640.0 \pm 216.0	104.0 \pm 7.6
S xiii	256.666	802.0 \pm 108.0	62.6 \pm 4.7
Fe x + Si ix	257.246	166.0 \pm 41.7	47.4 \pm 8.6
Fe xiv (+ Ar xiv)	257.370	295.0 \pm 96.3	63.8 \pm 15.1
Si ix	258.077	170.0 \pm 49.2	89.9 \pm 18.9
Si x	258.361	379.0 \pm 71.8	61.0 \pm 7.7
S x	259.465	216.0 \pm 66.9	54.5 \pm 12.2
Si x	261.043	265.0 \pm 66.9	120.0 \pm 21.4
Fe xvi	262.965	858.0 \pm 104.0	64.5 \pm 4.0
Fe xiv	264.768	1270.0 \pm 156.0	70.9 \pm 4.5
.....	265.820	115.0 \pm 41.6	48.8 \pm 12.9
Fe xiv	270.511	674.0 \pm 118.0	80.2 \pm 9.1
Fe xiv	274.193	1360.0 \pm 176.0	69.9 \pm 4.9
.....	280.496	180.0 \pm 46.9	58.5 \pm 10.8
(S xi)	281.364	208.0 \pm 79.8	93.0 \pm 26.2
Fe xv	284.151	13900.0 \pm 1590.0	66.8 \pm 3.5
S xi	285.820	132.0 \pm 44.3	42.7 \pm 10.6
S xii	288.415	203.0 \pm 54.7	64.2 \pm 12.3
.....	288.588	102.0 \pm 34.4	41.6 \pm 10.2
Fe xiv	289.140	213.0 \pm 46.4	62.7 \pm 9.4
Ni xviii	291.983	481.0 \pm 68.7	74.8 \pm 6.3
Si ix	292.756	126.0 \pm 49.3	46.9 \pm 14.1
Si ix	292.858	61.6 \pm 44.2	46.6 \pm 26.9
Si ix + Fe vi	296.102	179.0 \pm 46.4	54.4 \pm 10.0
Si xi	303.317	3360.0 \pm 386.0	89.2 \pm 4.8
He ii	303.782	36000.0 \pm 4070.0	86.4 \pm 4.4
Mn xiv (+ Fe xv)	304.868	216.0 \pm 60.3	79.0 \pm 15.8
Fe xi + Fe vi	308.545	120.0 \pm 37.4	73.9 \pm 16.7
Fe xiii	312.167	172.0 \pm 33.8	48.7 \pm 6.5
Mg viii	315.029	144.0 \pm 46.4	51.3 \pm 12.0
Mg viii	317.023	62.1 \pm 25.7	43.3 \pm 13.4
Fe xiii	318.100	112.0 \pm 42.8	63.5 \pm 17.8
Mg vii + Ni xv	319.002	227.0 \pm 51.2	95.0 \pm 14.9
Fe xiii	320.796	195.0 \pm 57.8	67.0 \pm 14.3
Al x	332.782	173.0 \pm 44.1	66.3 \pm 11.9
Fe xiv	334.167	923.0 \pm 107.0	73.7 \pm 4.0
Fe xvi	335.401	12000.0 \pm 1350.0	78.4 \pm 4.0

NOTE.—Intensities are in $\text{ergs cm}^{-2} \text{s}^{-1} \text{sr}^{-1}$

northeast were obtained in the second pointing position. We used the longest exposure in this position (202.4 s) to obtain the active region spectrum given in Table 2.

Following Brosius et al. (1997a), we derived the absolute pointing of the SERTS-95 observations by co-aligning our He ii $\lambda 304$ spectroheliograms with coordinated, full disk He i $\lambda 10830$ images from the NSO/KPNO Spectro-magnetograph. We found that the center of the SERTS entrance aperture assembly projected onto a point located $213'' \pm 7''$ west and $483'' \pm 7''$ north of solar disk center (in the quiet Sun) for the first pointing position, and $335'' \pm 7''$ west and $198'' \pm 7''$ north (in region 7870) for the second. The narrow slit bisected NOAA region 7870 at a $24^\circ 3' \pm 0^\circ 2'$ angle counterclockwise from the solar rotation axis.

Spectra are available for each $4''.42$ spatial pixel along the narrow slit; however, for the present work we averaged over the $3''.76$ segment corresponding to region 7870 in order to enhance the signal-to-noise ratio and therefore acquire as many spectral lines as possible for calibration and density analyses. For the quiet-Sun spectrum, we averaged over the entire $5'$ slit for the same reason. Each averaged spectrum exhibits a background level owing to film fog, scattered light, and actual solar continuum. We calculated this background for each averaged spectrum by removing strong spectral features (emission-line candidates) from the initial spectrum, replacing them with appropriate local averages, and smoothing the remainder. The backgrounds derived in this way were then subtracted from the initial spectra,

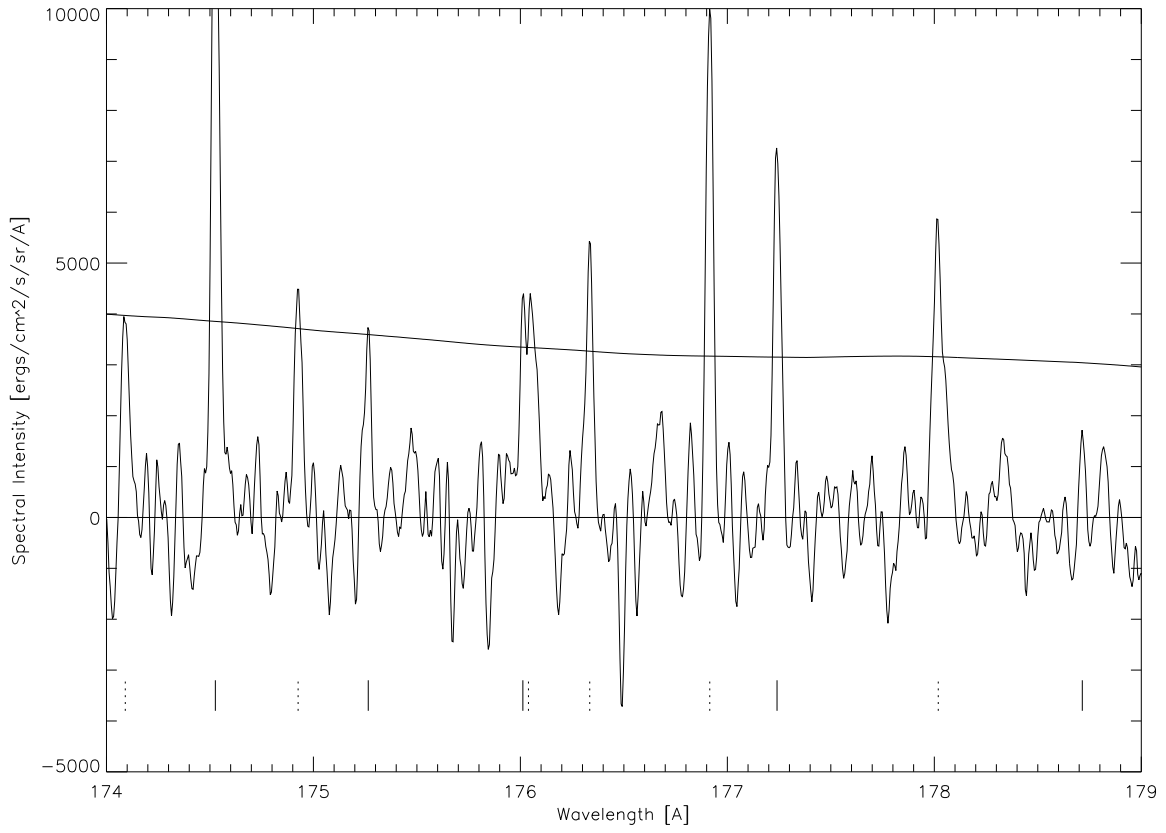


FIG. 1a

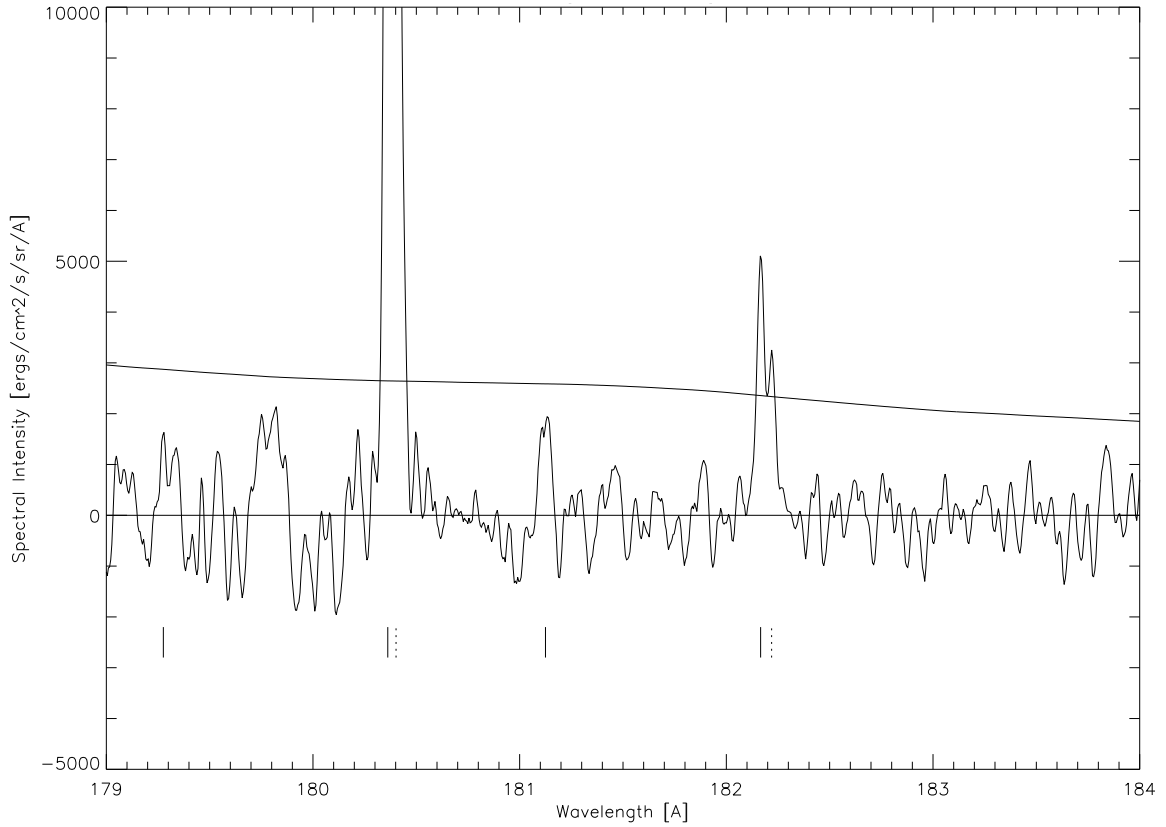


FIG. 1b

FIG. 1.— (a)–(j) The SERTS-95 second-order active region spectrum in 5 Å bins. (k)–(t) The first-order spectrum in 10 Å bins. The entire spectrum in this figure has been smoothed with a five-point running boxcar. Lines that appear off scale are not saturated; the vertical scale was chosen to allow the weaker lines to be visible. A curve showing 3 times the standard deviation in the local background noise ($3\sigma_B$, representing the nominal spectral intensity minimum for real spectral features) is overplotted for reference. Solid vertical lines in (a)–(j) indicate second-order lines that are included in Table 2; dotted vertical lines indicate first-order lines that are not included. Solid vertical lines in (k)–(t) indicate first-order lines that are included in Table 2.

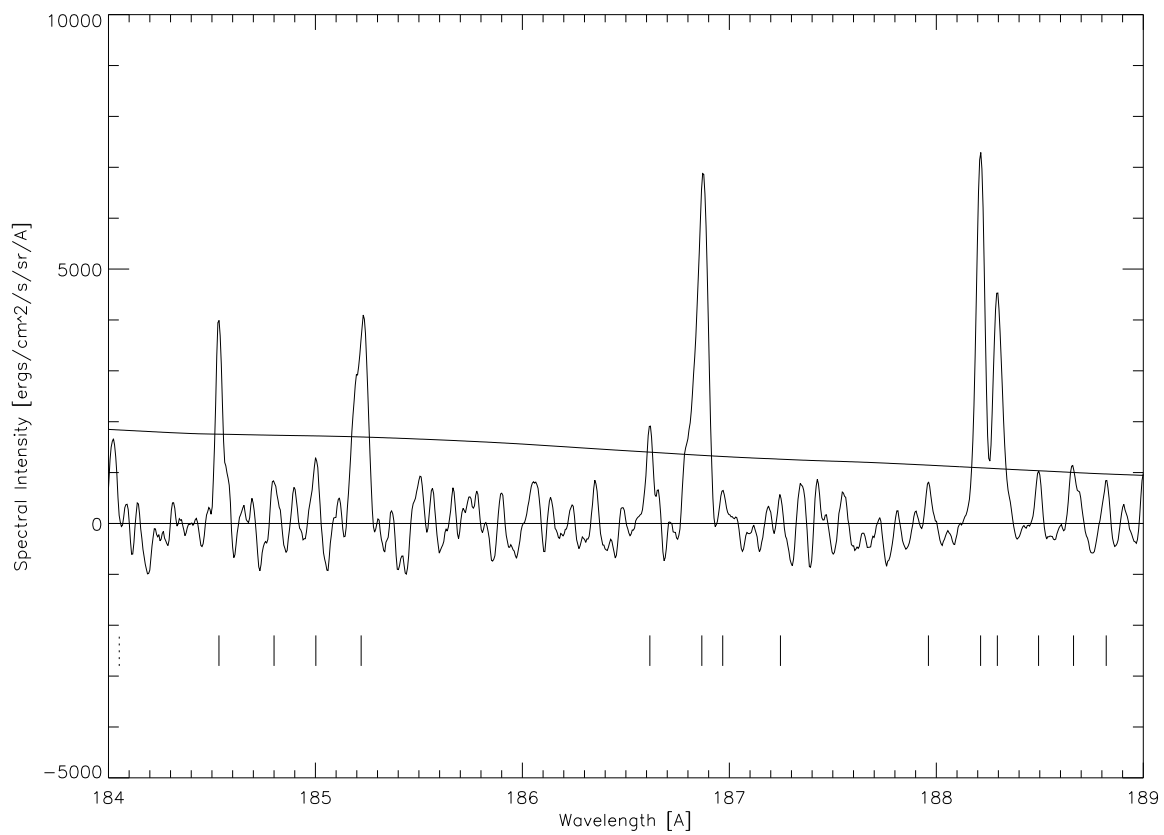


FIG. 1c

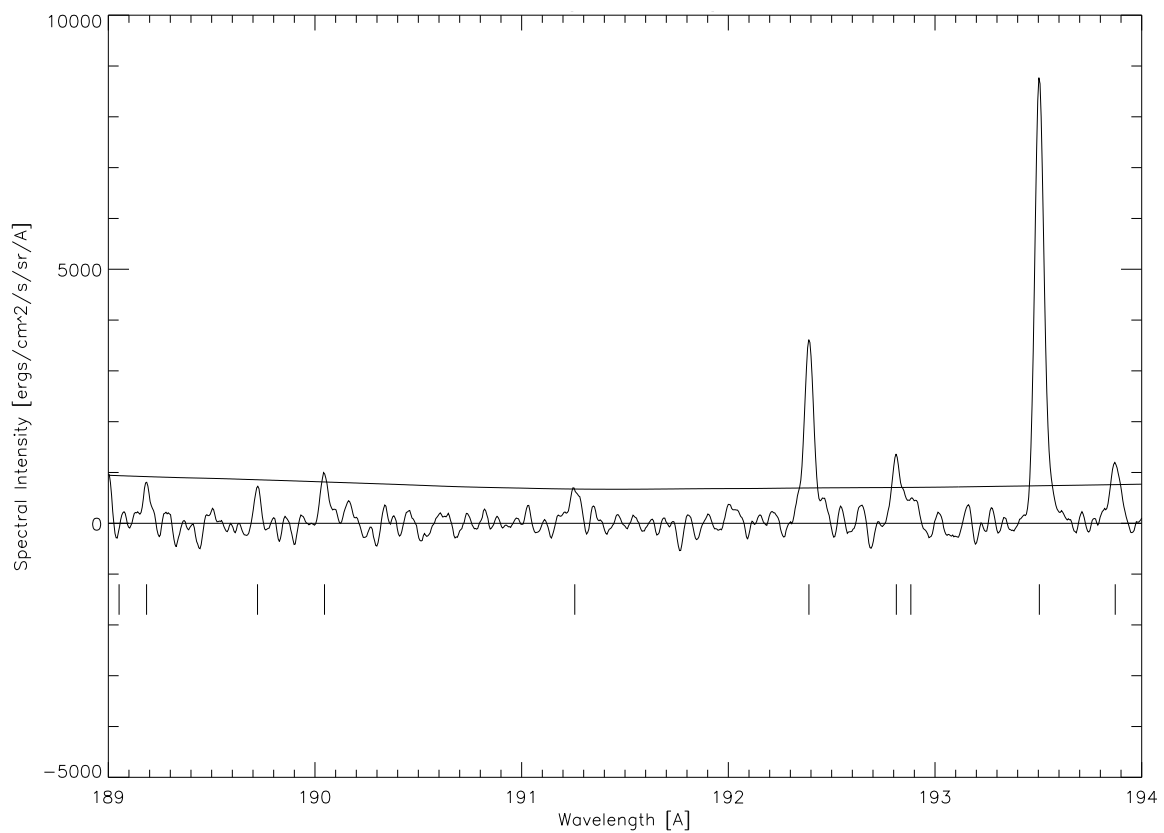


FIG. 1d

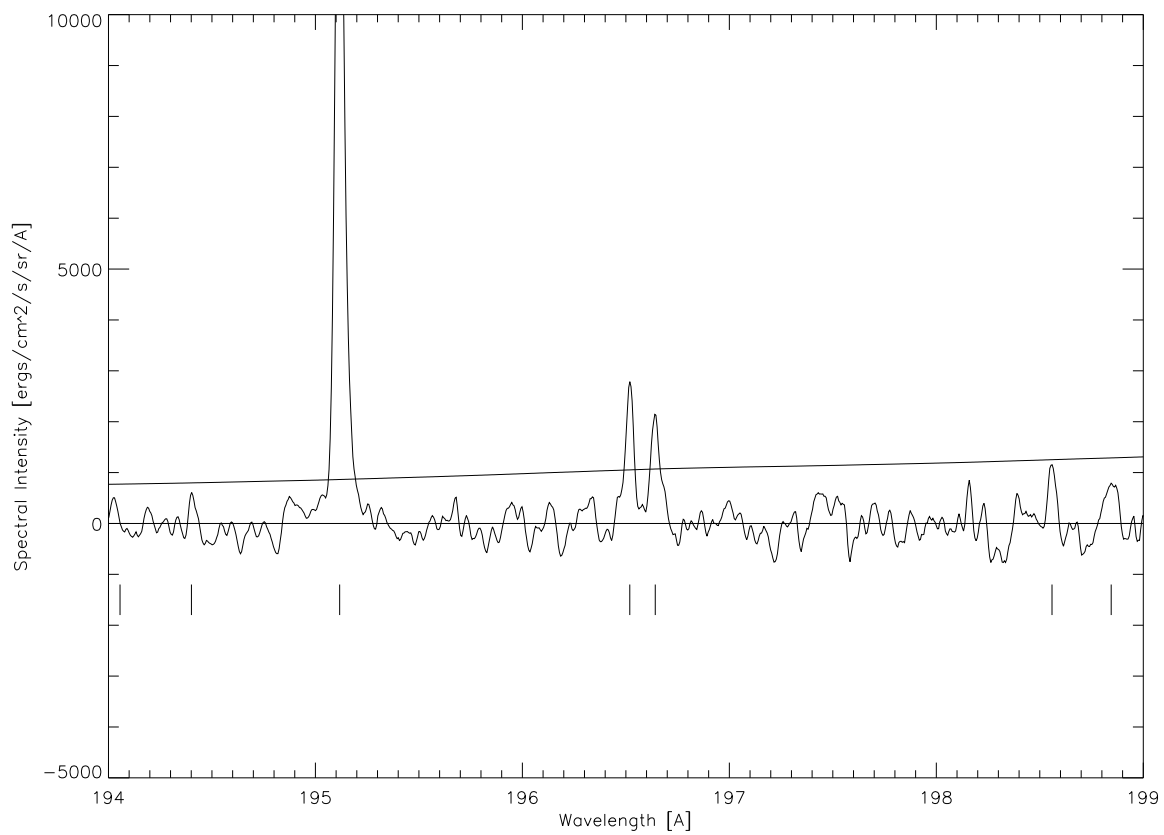


FIG. 1e

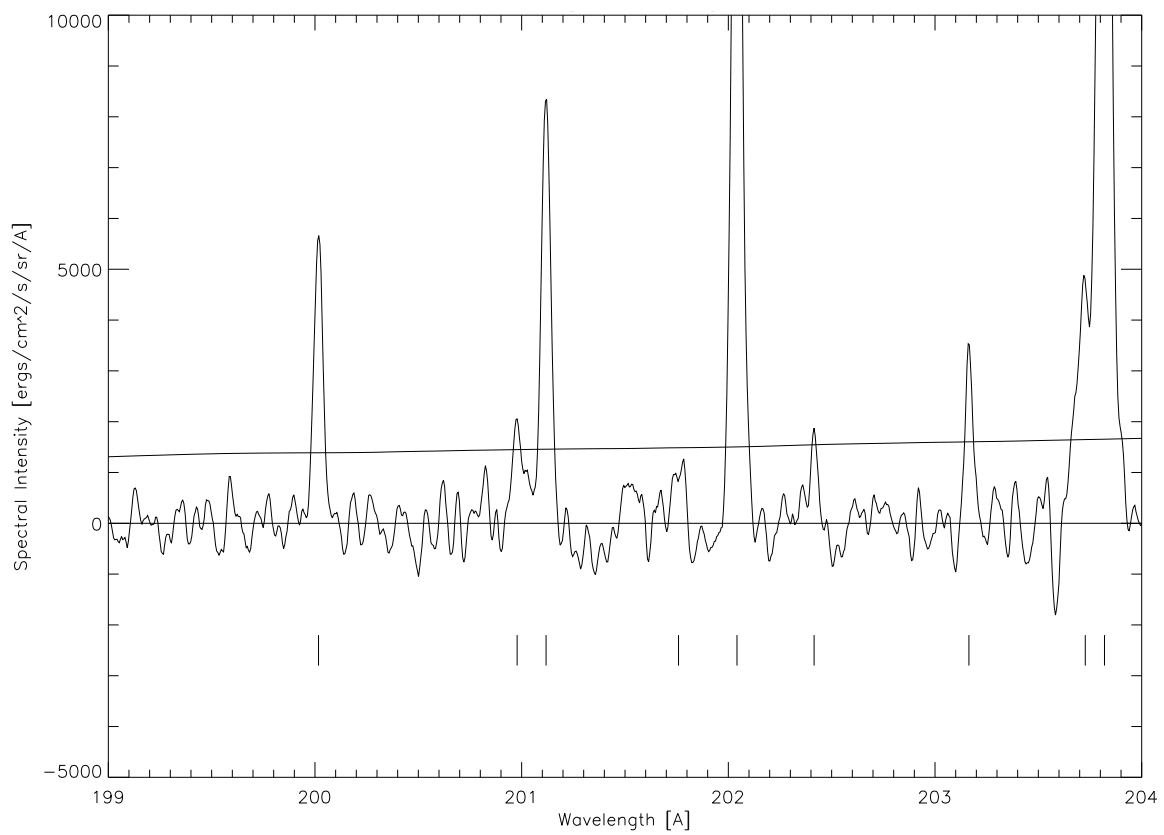


FIG. 1f

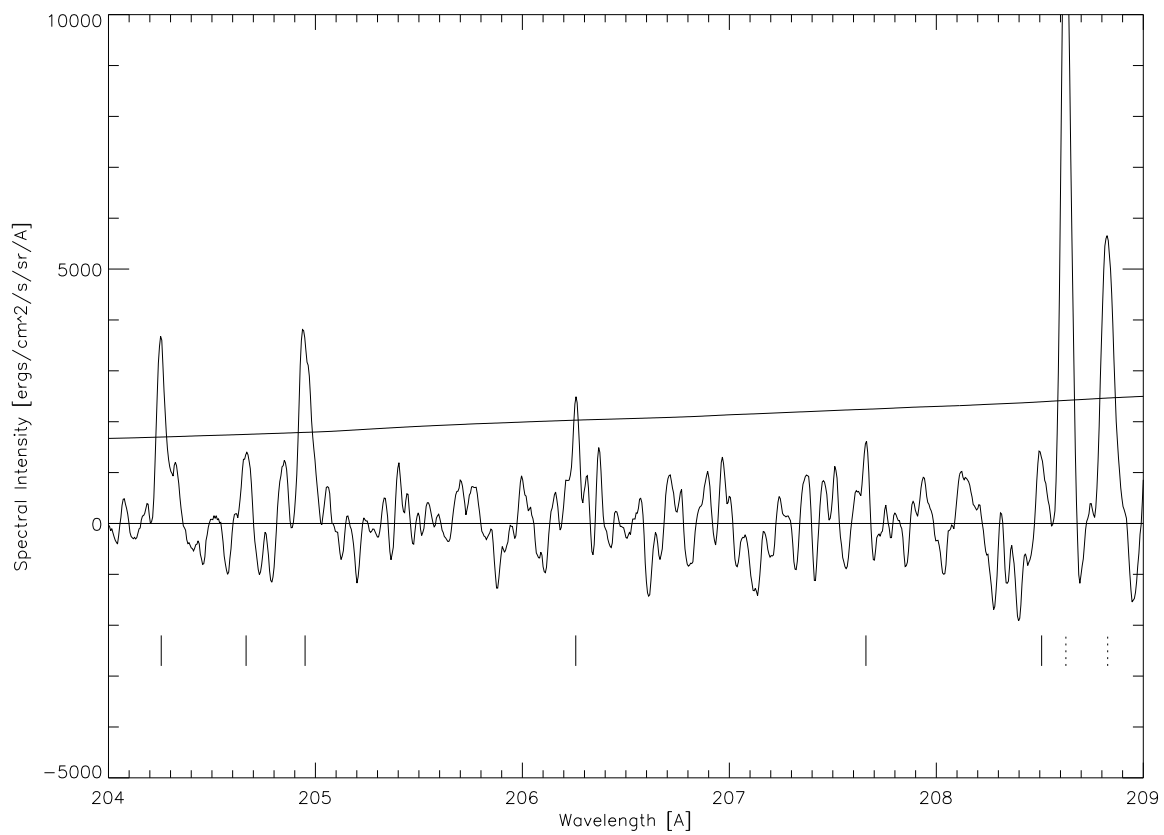


FIG. 1g

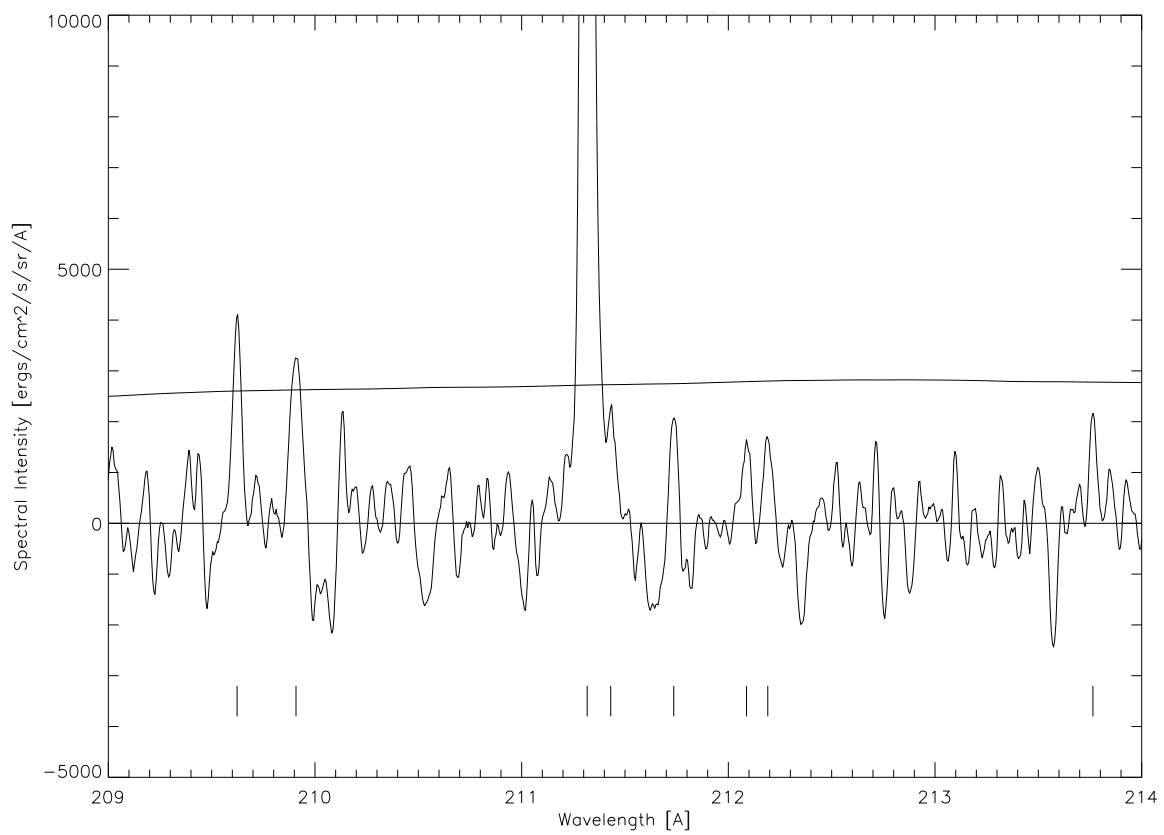


FIG. 1h

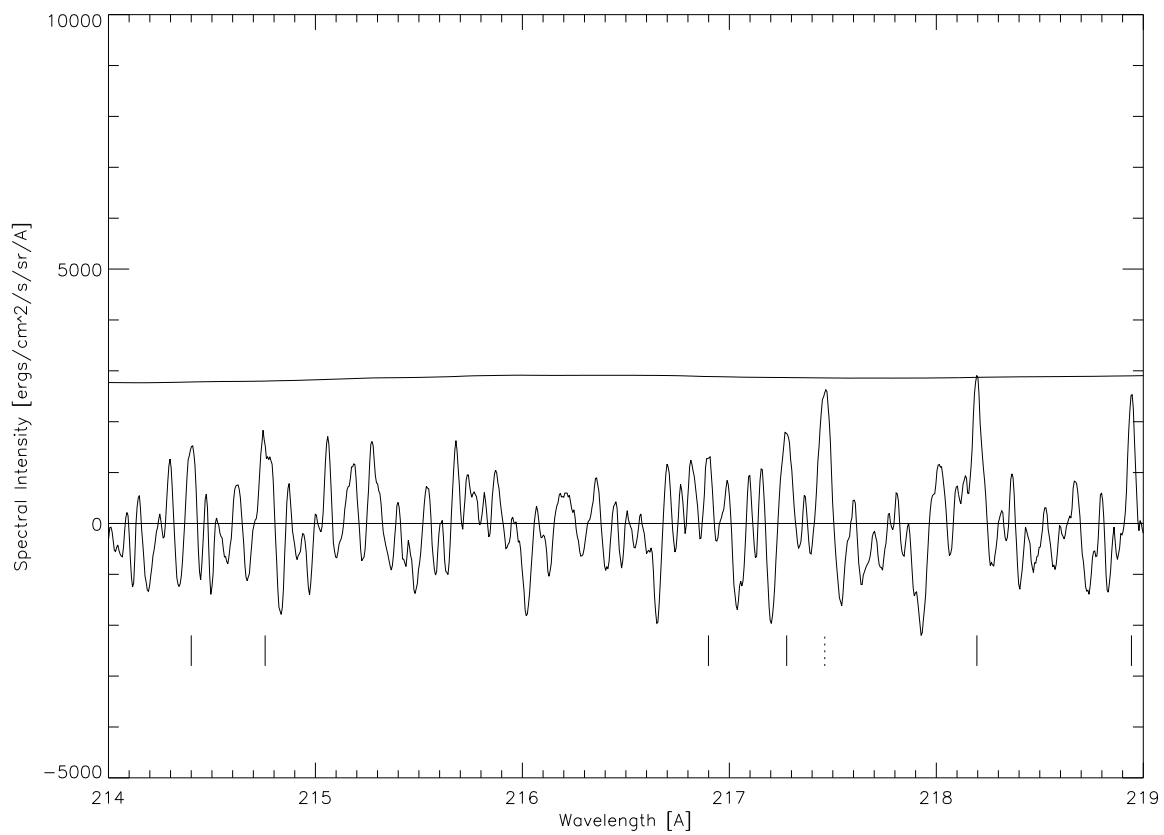


FIG. 1i

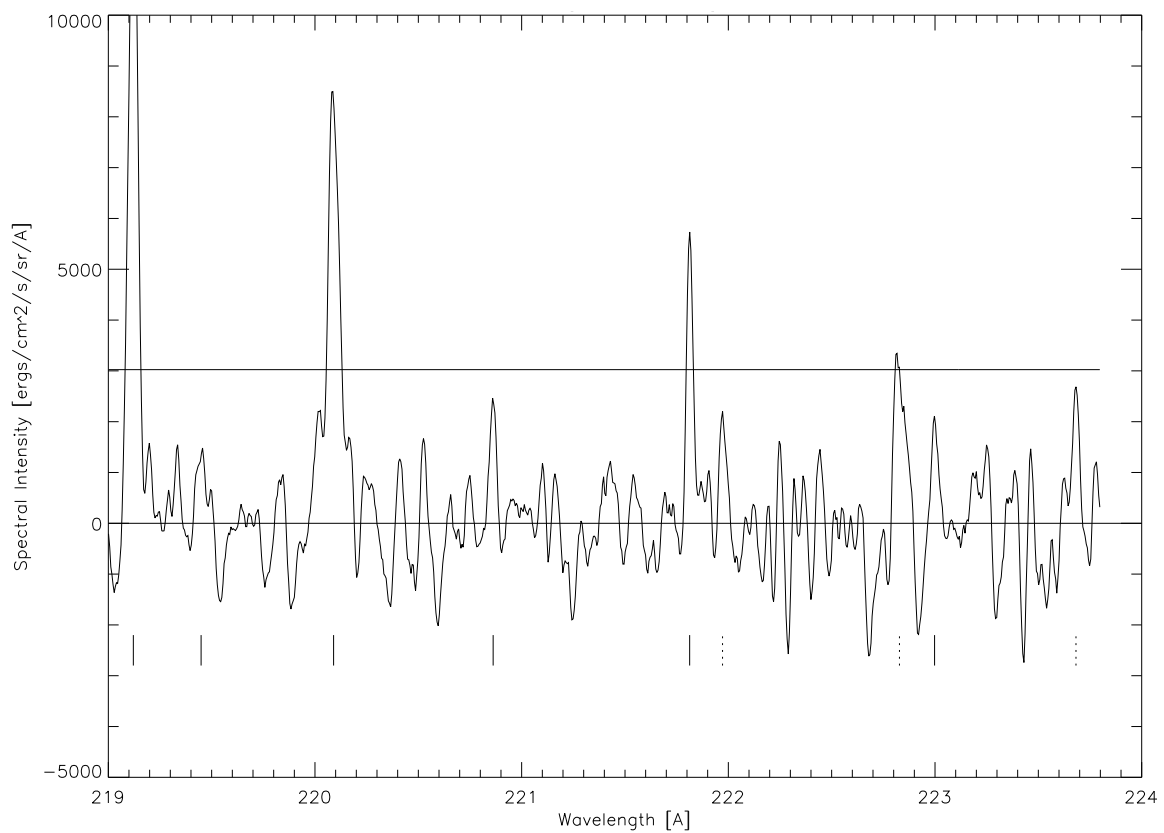


FIG. 1j

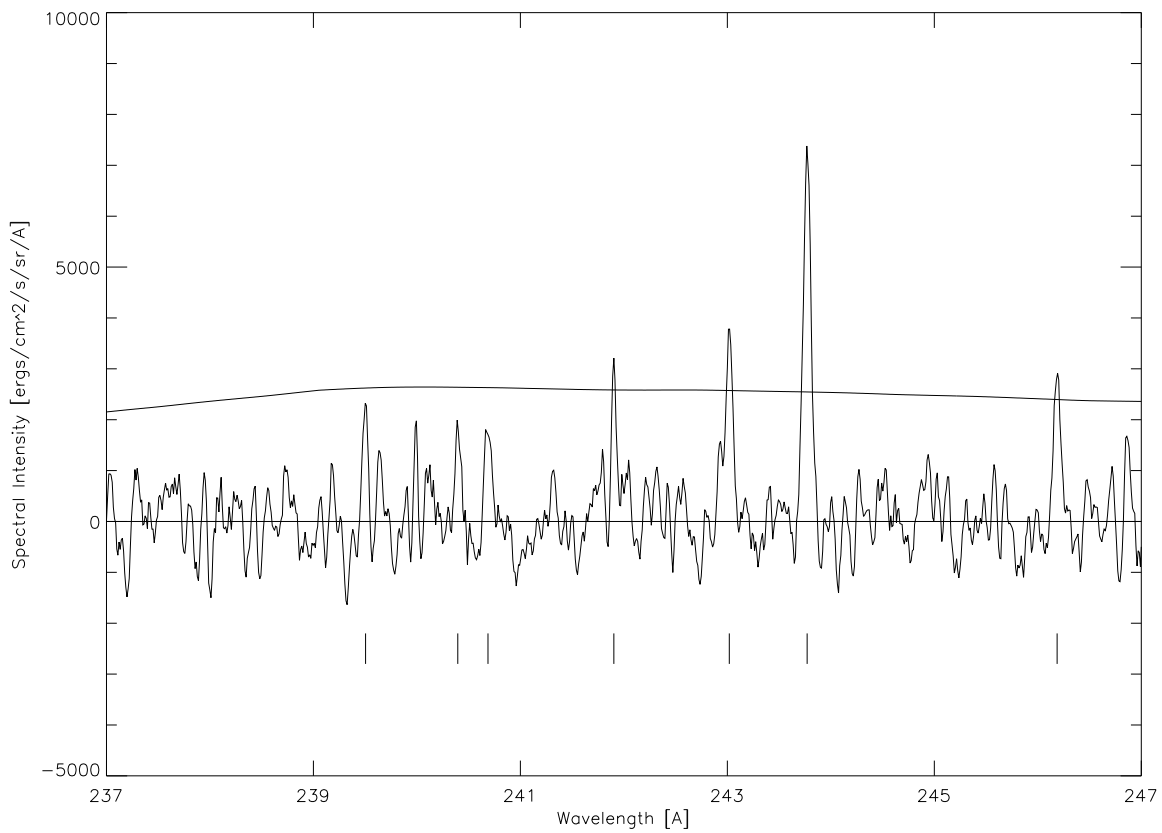


FIG. 1k

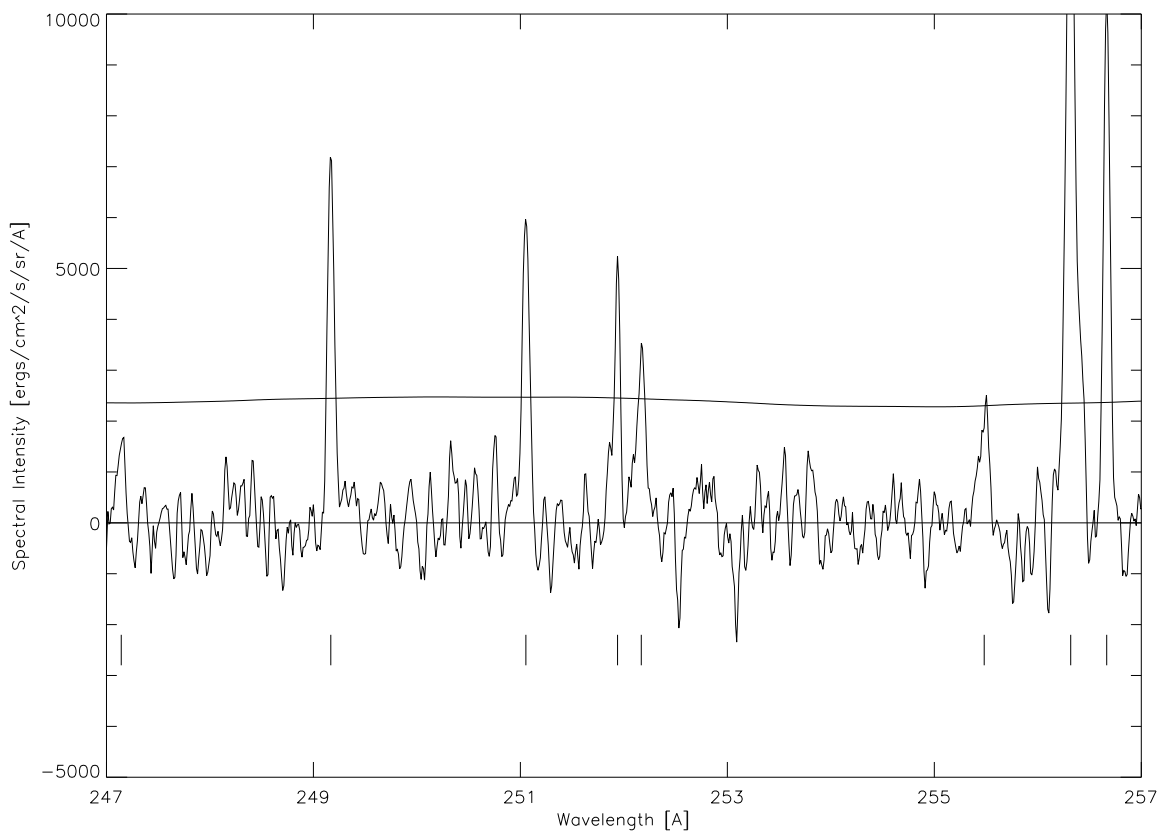


FIG. 1l

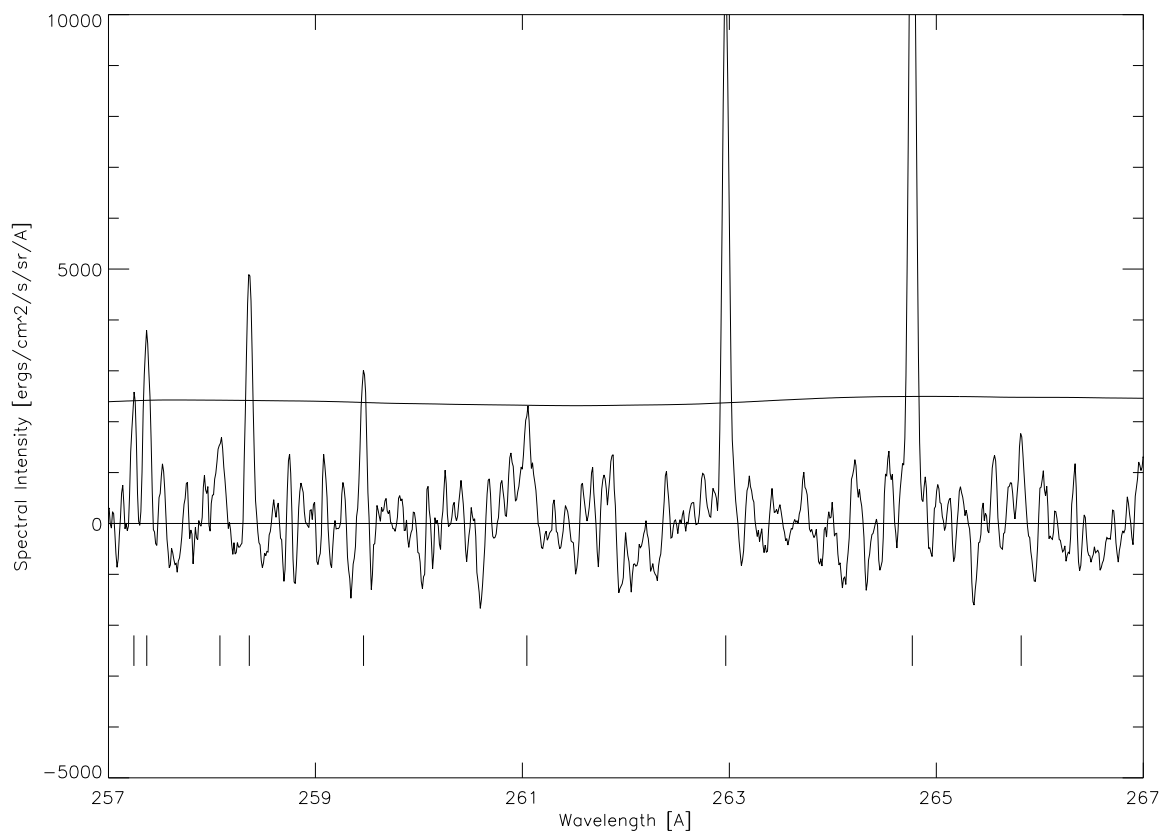


FIG. 1m

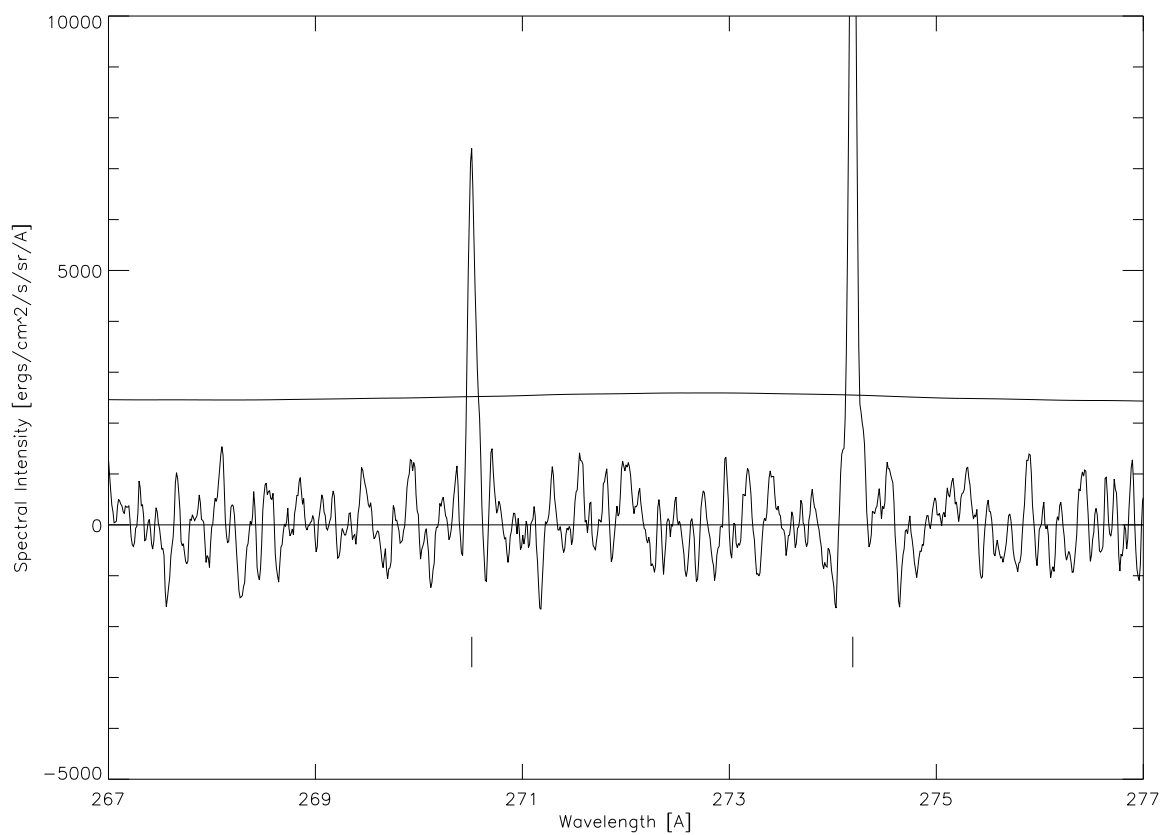


FIG. 1n

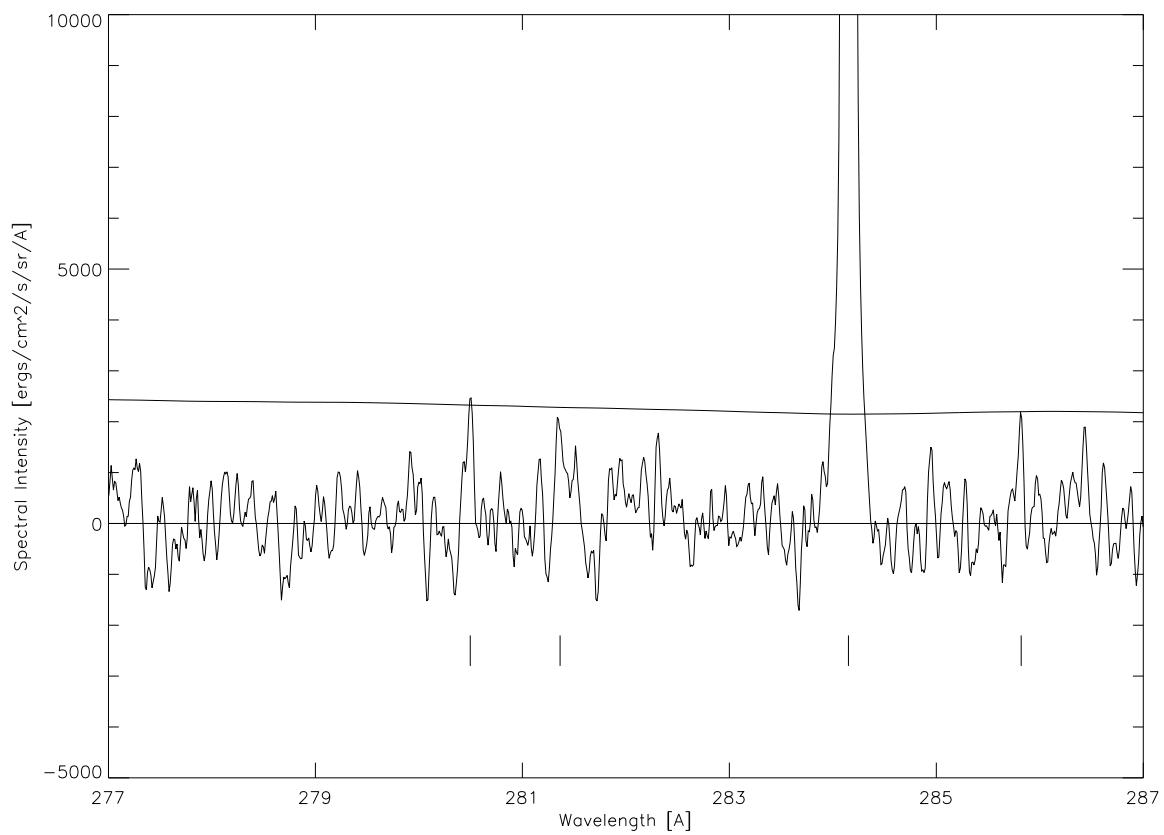


FIG. 1o

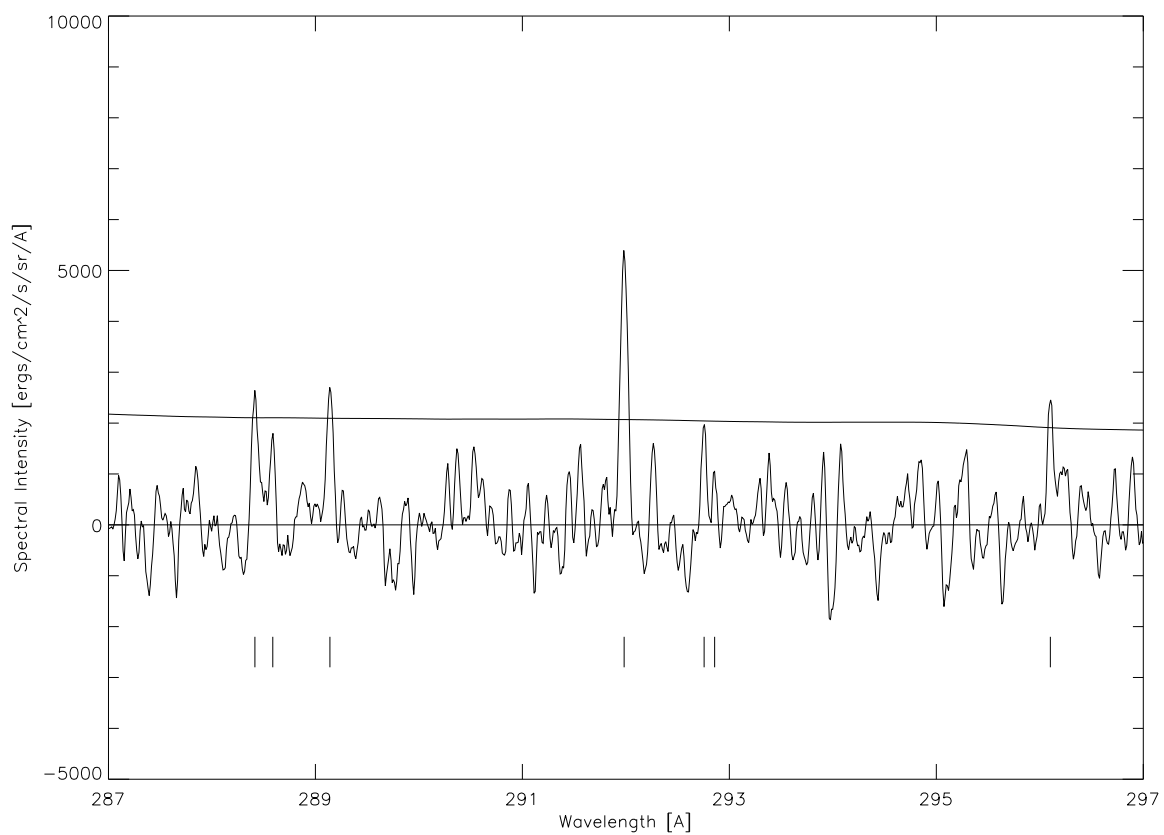


FIG. 1p

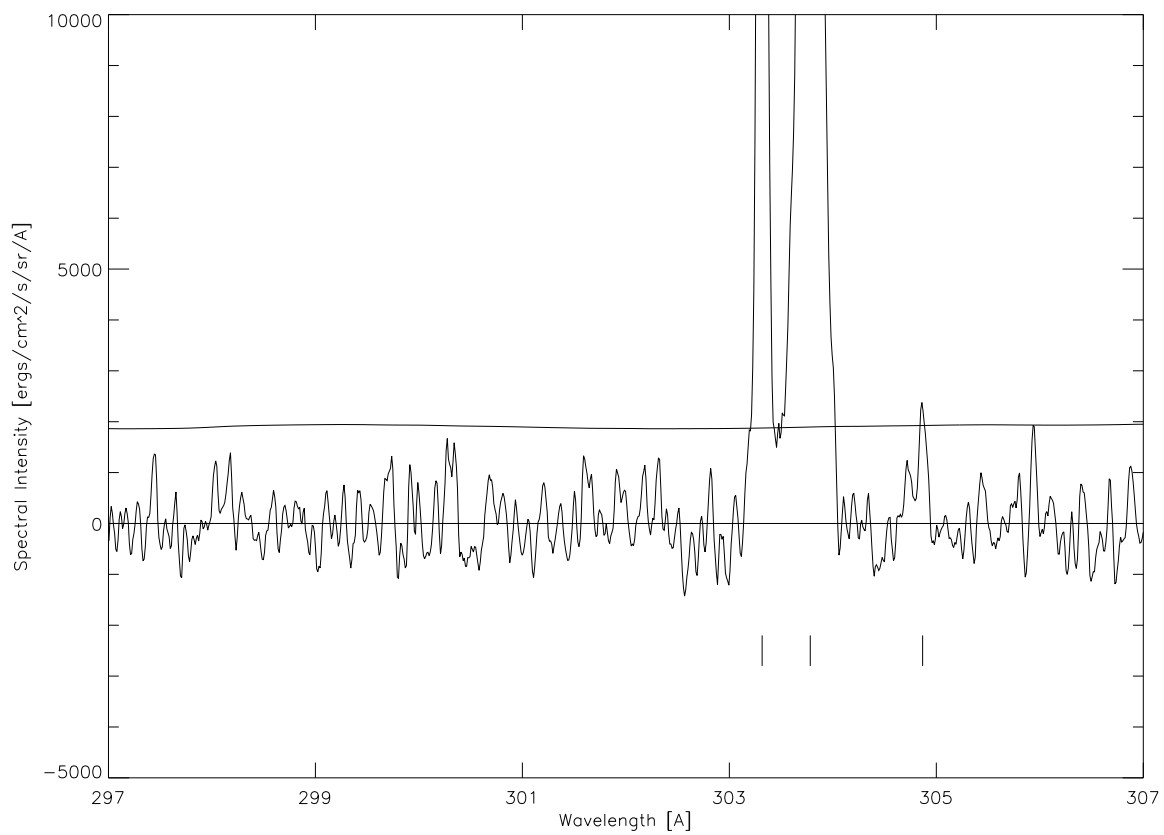


FIG. 1q

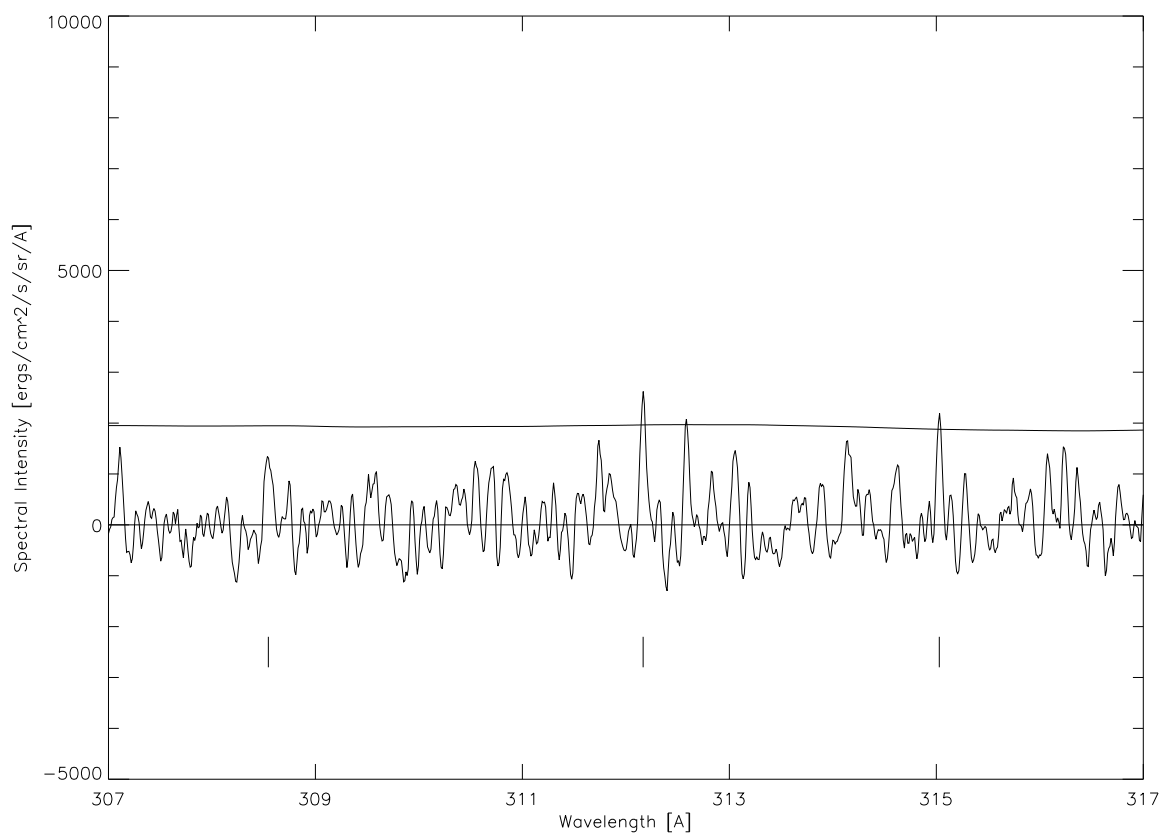


FIG. 1r

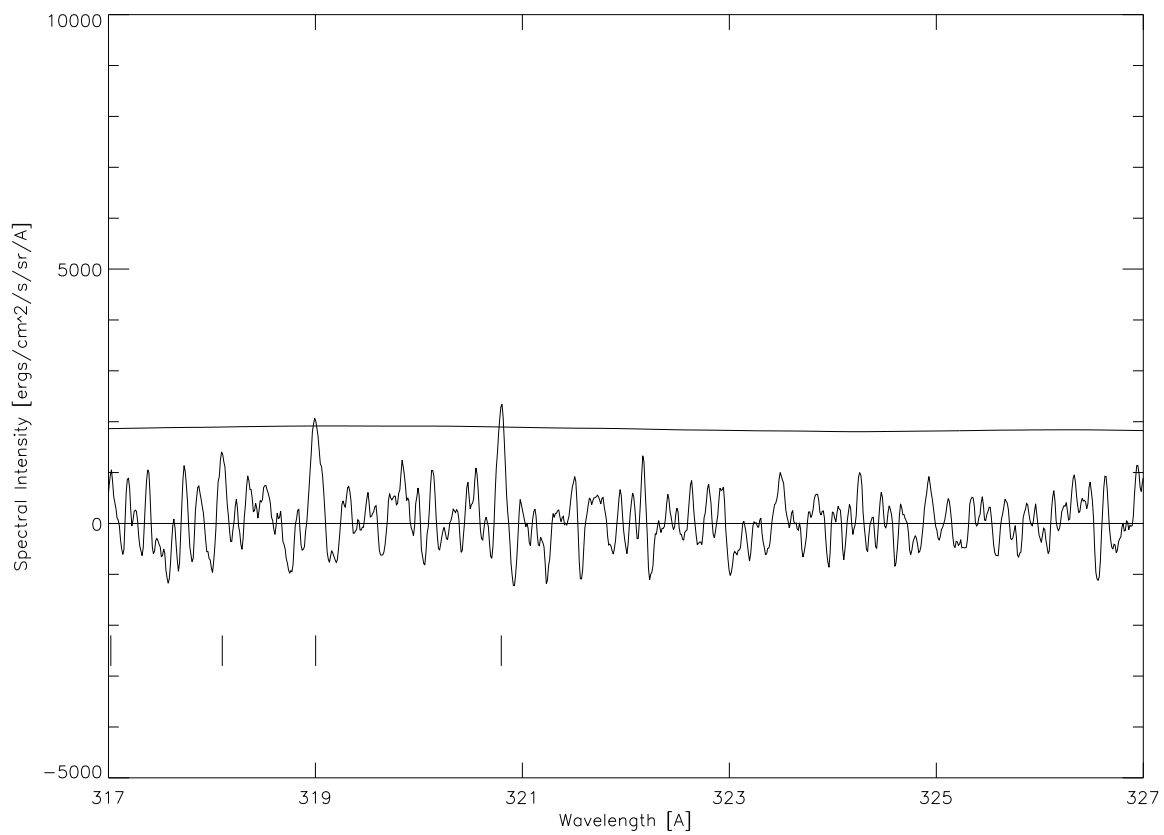


FIG. 1s

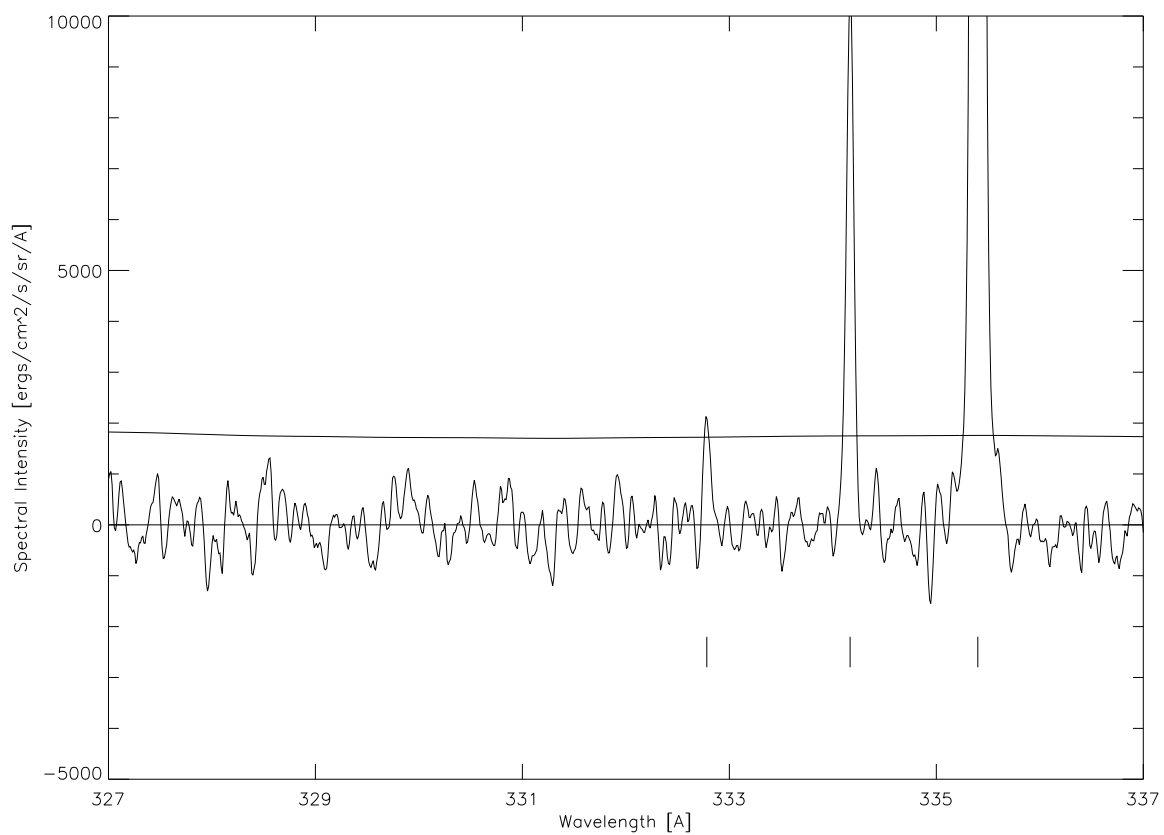


FIG. 1t

leaving only emission-line spectra (with noise) on a zero base level.

Lists of emission-line candidates for the active region and quiet-Sun spectra were compiled based upon the strength of the line candidates relative to the local background noise: candidates whose peak intensity was $\geq 3\sigma$ were included. In addition, second-order lines previously identified by Behring et al. (1976) or Dere (1978) were included in the candidate lists even if their peak intensities were somewhat low. The emission-line candidates in the background-corrected active region and quiet-Sun spectra were fitted with Gaussian profiles to obtain (1) the centroid wavelength, (2) the profile amplitude and its associated uncertainty, and (3) the Gaussian width and its associated uncertainty. The amplitude and Gaussian width were used to derive the integrated line intensity and the full width at half-maximum, as well as the uncertainty associated with each. An emission-line *candidate* is included as an actual *emission line* in Tables 1 and 2 if (1) the candidate's width (FWHM) plus its corresponding uncertainty exceeds the SERTS instrumental width (50–55 mÅ in first order, 25–27 mÅ in second order), (2) the candidate's integrated intensity exceeds twice its associated uncertainty, and (3) the candidate's profile visibly resembles that of an emission line. The latter is a somewhat subjective criterion and may lead to the exclusion of some very weak lines from the tables.

Figure 1 shows the SERTS-95 absolutely calibrated, background-corrected, average active region spectrum, smoothed with a five-point running boxcar. (The line lists in Tables 1 and 2 were obtained from unsmoothed spectra.) A horizontal line at zero intensity is shown for reference. Also included for reference is a curve showing 3 times the standard deviation in the local background noise ($3\sigma_B$). Lines included in Table 2 are indicated with solid vertical lines at the appropriate wavelength. Dotted vertical lines indicate first-order lines for which the uncertain calibration precluded the lines' inclusion in Table 2.

3. CALIBRATION

The efficiency of the SERTS-95 multilayer-coated grating was directly measured at the Synchrotron Ultraviolet Radiation Facility of the National Institute of Standards and Technology (NIST). Unfortunately, the configuration of that facility at the time was not well suited for separating the multiple-order response of our grating, and so a reliable, usable calibration curve could not be derived. We therefore used available density- and temperature-insensitive line intensity ratios from the spatially averaged solar active region spectrum itself in order to derive the SERTS-95 relative radiometric calibration. Such an approach was proposed by Neupert & Kastner (1983) as a means of monitoring relative calibration variations of in-flight EUV spectrometers and was used by Brosius et al. (1996a) to adjust the laboratory calibration curve for SERTS-91 and SERTS-93. Brosius et al. (1998) present results of this calibration technique for the second-order wave band only (170–225 Å), using the SERTS-95 active region spectrum; in the present work we extend the procedure to cover the first-order wave band. A related line diagnostic technique was developed and applied by Landi et al. (1998b) to derive correction factors for *SOHO*'s CDS/NIS. The SERTS data and analysis procedure described here should be helpful for ongoing CDS calibration efforts (see, e.g., Landi et al. 1998a).

We used the CHIANTI package (version 1.01; Dere et al. 1997) to obtain theoretical values for density- and temperature-insensitive line intensity ratios among emission lines observed by SERTS-95. These include lines from Fe x through Fe xvi, and He II. For Fe xiv, we used more recent calculations provided by P. J. Storey (1998, private communication). The lines used in this work are listed in Table 3, in which the first two columns identify the line by ion and wavelength, and the third column provides the theoretical intensity (in energy units) normalized to one of the lines in each given series. Some of the line intensity ratios exhibit slight variations with density. These are indicated as uncertainties on the normalized theoretical intensities, where the uncertainty corresponds to half of the difference between the maximum and minimum values within the range $8.5 \leq \log n_e \leq 10.5$. In each case the intensity ratios were calculated at the temperature of maximum ion abundance (i.e., the lines' "formation temperature"), using the Arnaud & Raymond (1992) ionization equilibrium calculations. (Using the Arnaud & Rothenflug 1985 ionization equilibrium calculations produces no change.)

The SERTS-95 relative radiometric calibration was derived by obtaining factors by which the various integrated line intensities in the spatially averaged, uncalibrated active region spectrum must be multiplied in order to obtain agreement between the observed and the theoretical line intensity ratios. The derived first- and second-order factors were fitted with smooth curves and were normalized to the sensitivity at the He II $\lambda 303.782$ line. Because effects due to atmospheric absorption, the reflectivity of the telescope, and the transmission of the aluminum filter all vary smoothly and gradually with wavelength, the overall shape of the instrumental response curve derived here is dominated by that of the multilayer coating. The peak response occurs at 192 Å in the second-order wave band and diminishes rapidly with distance from this wavelength. The resulting instrumental relative response is shown in Figure 2.

The derived instrumental relative response curve was applied to the original uncalibrated active region and quiet-Sun spectra, thus yielding relatively calibrated spectra. We then placed the relatively calibrated spectra onto an absolute intensity scale by forcing our quiet-Sun He II $\lambda 303.8$ + Si XI $\lambda 303.3$ intensity to match results of Mango et al. (1978). Mango et al. combined sounding rocket observations (Heroux, Cohen, & Higgins 1974; Higgins 1976) with *OSO-3* (Chapman & Neupert 1974) and *OSO-7* (Linsky et al. 1976) observations to deduce a limb-brightening expression for the absolute intensity of this *combination* because the observations were unable to resolve the blend. The SERTS-95 quiet-Sun slit was centered on a position angle $\sim 34^\circ$ relative to disk center (i.e., $\mu = \cos \theta = 0.83$). For this position, the results of Mango et al. (1978) yield a Si XI + He II intensity of $7488 \text{ ergs cm}^{-2} \text{ s}^{-1} \text{ sr}^{-1}$. From the quiet-Sun SERTS spectroheliograms, which cover an area of $300'' \times 480''$, we find that the Si XI + He II intensity averaged over the slit position (which covers an area of $300'' \times 5''$) is 27% greater than that averaged over the entire corresponding image. Thus we require that the SERTS Si XI $\lambda 303.3$ + He II $\lambda 303.8$ quiet-Sun slit intensity be $7488 \times 1.27 = 9510 \text{ ergs cm}^{-2} \text{ s}^{-1} \text{ sr}^{-1}$. Since SERTS is able to resolve the Si XI + He II blend, and since the Si XI line is absent from the 1995 quiet-Sun spectrum, the intensity of the quiet-Sun He II $\lambda 303.8$ line *alone* must be $9510 \text{ ergs cm}^{-2}$

TABLE 3
LINES USED TO DERIVE THE SERTS-95 RELATIVE RADIOMETRIC CALIBRATION

Ion (1)	Wavelength (2)	Normalized Theoretical <i>I</i> (3)	Normalized Observed. <i>I</i> (4)	Normalized Observed/ Theoretical (5)
He II	243.019	0.0081 ± 0.0004	0.0090 ± 0.0022	1.0937 ± 0.2700
	303.782	1.0000 ± 0.0000	1.0000 ± 0.1129	0.9841 ± 0.1111
Fe X	174.526	1.0000 ± 0.0000	1.0000 ± 0.1269	1.0621 ± 0.1348
	177.240	0.6190 ± 0.0140	0.5114 ± 0.0974	0.8775 ± 0.1683
	184.534	0.2560 ± 0.0100	0.2498 ± 0.0483	1.0366 ± 0.2043
	190.046	0.0776 ± 0.0029	0.0732 ± 0.0171	1.0016 ± 0.2365
Fe XI	181.125	0.4020 ± 0.0180	0.5189 ± 0.1669	1.3023 ± 0.4229
	182.166	1.0000 ± 0.0000	1.0000 ± 0.1410	1.0089 ± 0.1422
	189.722	0.1390 ± 0.0320	0.1114 ± 0.0324	0.8084 ± 0.2998
Fe XI	188.214	1.0000 ± 0.0000	1.0000 ± 0.2006	0.9575 ± 0.1920
	192.813	0.2090 ± 0.0000	0.2412 ± 0.0659	1.1051 ± 0.3018
Fe XII	186.867	3.5800 ± 0.4400	4.1381 ± 0.8162	1.1586 ± 0.2693
	196.642	1.0000 ± 0.0000	1.0000 ± 0.1495	1.0023 ± 0.1499
	219.449	0.7650 ± 0.0390	0.6198 ± 0.2163	0.8121 ± 0.2864
Fe XII	192.390	0.2120 ± 0.0020	0.2370 ± 0.0397	1.0797 ± 0.1812
	193.505	0.5540 ± 0.0440	0.5604 ± 0.0907	0.9770 ± 0.1762
	195.117	1.0000 ± 0.0000	1.0000 ± 0.1152	0.9660 ± 0.1113
	211.736	0.0868 ± 0.0137	0.1084 ± 0.0358	1.2067 ± 0.4414
Fe XIII	200.017	1.0000 ± 0.0000	1.0000 ± 0.1207	1.0951 ± 0.1322
	203.164	0.5140 ± 0.0910	0.5073 ± 0.1004	1.0809 ± 0.2870
	203.820	5.1800 ± 0.2100	6.3244 ± 1.0919	1.3371 ± 0.2371
	204.255	0.6520 ± 0.0690	0.6396 ± 0.1244	1.0742 ± 0.2379
	209.623	0.7520 ± 0.0410	0.6886 ± 0.1369	1.0028 ± 0.2067
	221.813	1.1800 ± 0.1300	0.7168 ± 0.1375	0.6652 ± 0.1471
	320.796	0.5460 ± 0.0110	0.6390 ± 0.2049	1.2816 ± 0.4117
Fe XIII	202.042	1.0000 ± 0.0000	1.0000 ± 0.1133	0.9844 ± 0.1115
	209.908	0.1700 ± 0.0000	0.1852 ± 0.0416	1.0726 ± 0.2408
Fe XIII	201.118	1.0000 ± 0.0000	1.0000 ± 0.1289	0.9215 ± 0.1188
	204.950	0.2930 ± 0.0000	0.5687 ± 0.1197	1.7885 ± 0.3764
Fe XIII	240.687	0.4110 ± 0.0000	0.6522 ± 0.2974	1.7873 ± 0.8148
	246.187	1.0000 ± 0.0000	1.0000 ± 0.1930	1.1262 ± 0.2173
	251.939	1.8790 ± 0.0000	1.3500 ± 0.3711	0.8091 ± 0.2224
Fe XIV	252.168	0.2420 ± 0.0000	0.2872 ± 0.0678	1.1518 ± 0.2721
	264.768	1.0000 ± 0.0000	1.0000 ± 0.1233	0.9706 ± 0.1197
Fe XIV	211.317	1.0000 ± 0.0000	1.0000 ± 0.1142	0.9675 ± 0.1105
	220.090	0.2110 ± 0.0000	0.2472 ± 0.0438	1.1333 ± 0.2009
	274.193	0.5400 ± 0.0200	0.5400 ± 0.0934	0.9675 ± 0.1711
	289.140	0.0481 ± 0.0018	0.0848 ± 0.0209	1.7050 ± 0.4245
	334.167	0.3940 ± 0.0360	0.3675 ± 0.0597	0.9024 ± 0.1683
Fe XV	243.771	0.0560 ± 0.0000	0.0480 ± 0.0092	0.8988 ± 0.1716
	284.151	1.0000 ± 0.0000	1.0000 ± 0.1140	1.0491 ± 0.1196
Fe XVI	251.053	0.0438 ± 0.0000	0.0435 ± 0.0079	1.0002 ± 0.1824
	262.965	0.0734 ± 0.0000	0.0716 ± 0.0119	0.9832 ± 0.1630
	335.401	1.0000 ± 0.0000	1.0000 ± 0.1129	1.0081 ± 0.1138

$\text{s}^{-1} \text{sr}^{-1}$ (see Table 1).

The observations used by Mango et al. were obtained either several years before or several years after the solar maximum of 1969 and so should be fairly representative of the declining phase of the solar cycle during which the SERTS-95 observations were obtained. The scatter in the Si XI + He II intensities used by Mango et al. to derive the center-to-limb variation was relatively small; however, we expect our absolute intensity calibration to be accurate only to a factor $\lesssim 2$ for the following reasons. Significant tem-

poral variations in the Si XI + He II full-Sun irradiances evident from the literature indicate that the quiet-Sun intensities are likely more variable than suggested by Mango et al. (1978). For example, the solar irradiance spectrum of Woods et al. (1998) can be integrated to yield a value of $3.3 \times 10^9 \text{ photons cm}^{-2} \text{ s}^{-1}$ during a period of low solar activity (1994 November 3). T. N. Woods² also reports values of 4.0×10^9 and 5.3×10^9 obtained during sounding

² At http://lasp.colorado.edu/rocket/rocket_results.html.

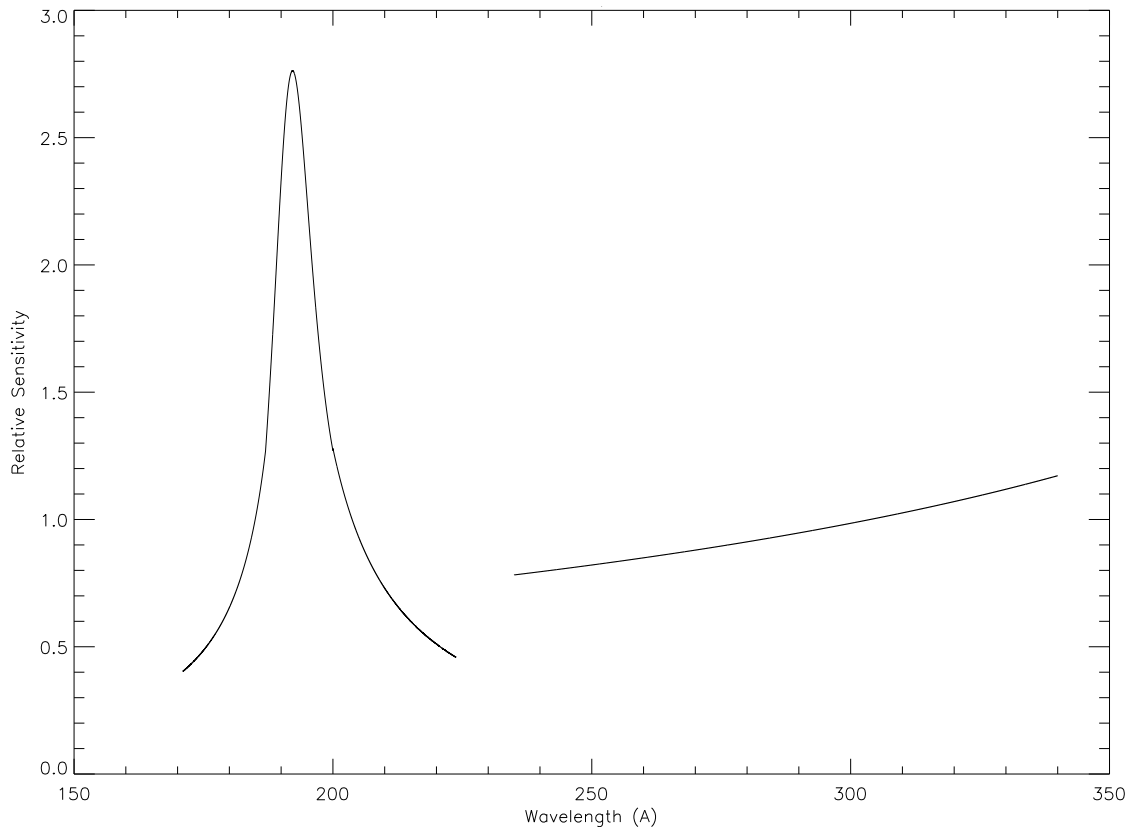


FIG. 2.—SERTS-95 relative radiometric response normalized to the value at He II $\lambda 303.782$, derived from density- and temperature-insensitive line intensity ratios. The narrow, sharply peaked curve centered on 192 Å in the second-order wave band is due to the multilayer coating on the toroidal diffraction grating.

rocket flights in 1993 and 1992, respectively. Ogawa et al. (1998) report a value of 4.7×10^9 based upon CELIAS/SEM observations from *SOHO* during solar minimum, and Timothy & Timothy (1970) give a value of 8.8×10^9 (comparable to values quoted in some of the references cited by Mango et al.) from *OSO-4* observations near the 1969 maximum. The maximum of the above irradiances is a factor of 2.67 greater than the minimum, which suggests variations by factors ~ 1.63 for irradiances during intermediate stages of the solar cycle. We therefore adopt a factor of 2 uncertainty on our absolute radiometric calibration.

The resultant observed integrated emission-line intensities (along with their associated measurement uncertainties) in *absolutely calibrated energy units* are listed in Tables 1 and 2. We have compensated for differences in atmospheric transmission between the different exposures used to obtain these lists. Because the He II $\lambda 303.782$ line is saturated in the longest active region exposure (202.2 s), we used the second longest active region exposure (40.4 s) to obtain this line's intensity.

Column (4) of Table 3 gives the observed intensity of a calibrated active region spectral line, relative to the "standard" line in its group. Ideally, the values listed in column (4) should match those listed in column (3). Column (5) gives the ratio of the observed intensities to the theoretical ones, normalized by the weighted average ratio within each group. Ratios close to unity indicate good agreement between the observed and the theoretical values. An inspection of column (5) in Table 3 reveals that all but four of the ratios agree to within their 1σ measurement uncertainties

and that *all* of them agree within factors better than 2. This is illustrated in Figure 3, where we plot the values in column (5) as a function of wavelength. The fact that no slope is evident in this figure indicates that there is no wavelength bias in the derived relative radiometric calibration. Further, the fact that so many line intensity ratios from seven successive ionization stages of iron yield mutually consistent results confirms the general validity of the atomic physics calculations.

We extrapolated the first-order calibration curve to wavelengths greater than 335.4 Å and obtained absolute intensities for the 19 first-order lines observed within the 336–364 and 417–447 Å wave bands. No first-order lines are observed between 365 and 417 Å (except possibly for a hint of the strong Mg IX line at 368 Å), which indicates that the second-order multilayer coating effectively precluded the detection of first-order lines corresponding to the wavelength range of greatest second-order sensitivity (~ 182 –208 Å). We examined the validity of the first-order line intensities in the extrapolated portion of the first-order wave band by comparing line intensity ratios involving one line from this regime and one line from the reliably calibrated regime with their corresponding theoretical values. We find that line intensity ratios that are too high by factors ~ 2 (e.g., Fe XII 338.290/196.642, Fe XII 346.841/195.117, Fe XII 364.439/195.117, and Fe XI 352.669/188.214) are intermixed with line intensity ratios that are too low by factors ~ 2 (e.g., Fe XVI 360.765/335.401) are intermixed with line intensity ratios that agree with theory (e.g., Fe XIV 353.829/219.121, Fe XIII 348.181/202.042, and Mg VIII

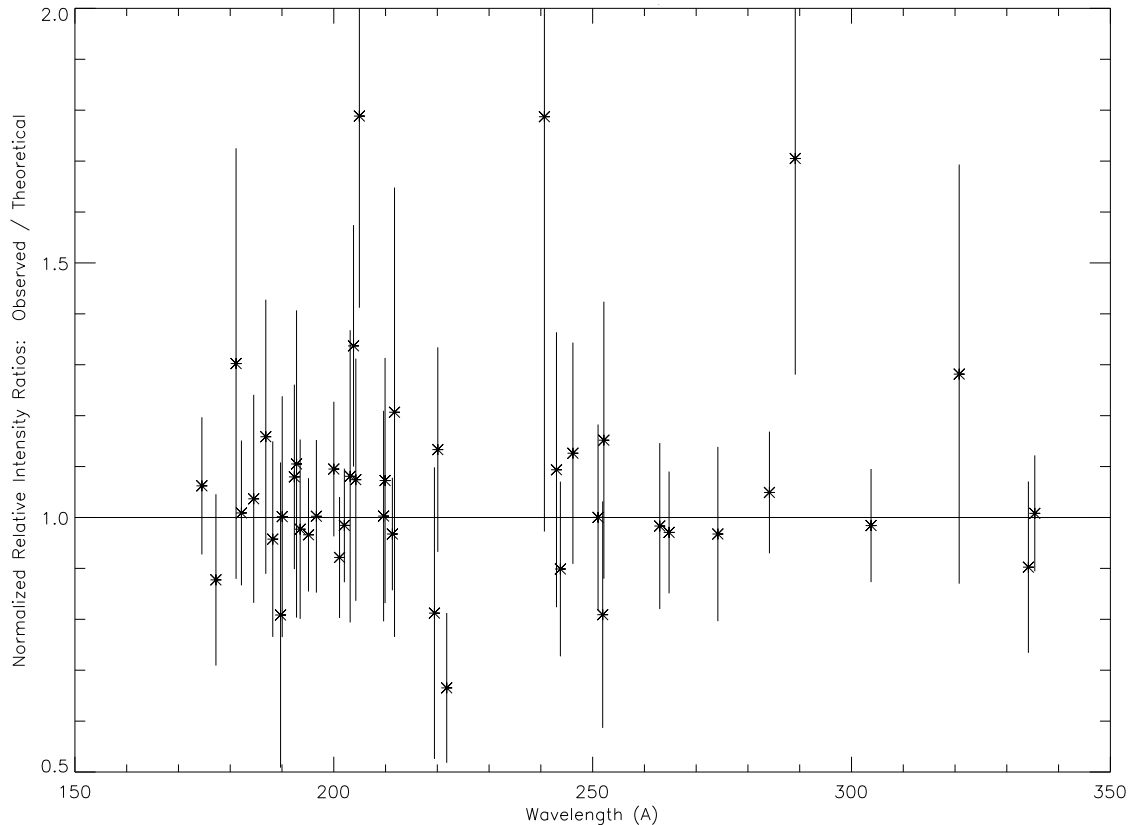


FIG. 3.—Plot of the ratio of the observed to theoretical intensity (Table 3, col. [5]), normalized to the weighted average ratio within each density- and temperature-insensitive line group in the active region spectrum, as a function of wavelength. Values close to unity indicate excellent agreement between observation and theory. The zero slope indicates that there is no wavelength bias in the derived calibration curve. The mutual consistency of the ratios demonstrates both the validity of the derived calibration and the accuracy of the atomic physics parameters.

339.006/315.029). This interspersal of line intensities that are too high, too low, and just right indicates complex behavior in the instrumental response near the edges of the multilayer wave band, and that we have insufficient data to establish the actual relative sensitivity in this wavelength region.

4. ACTIVE REGION SPECTRUM

A list of the 77 second-order emission lines and 50 first-order lines observed in NOAA active region 7870 is given in Table 2. This table provides a well-calibrated, high spectral resolution, representative solar active region spectrum, particularly for wavelengths in the SERTS-95 second-order wave band. It includes the line identification (where known), wavelength (in Å), integrated intensity with 1σ measurement uncertainty (in $\text{ergs cm}^{-2} \text{s}^{-1} \text{sr}^{-1}$), and full width at half-maximum intensity with 1σ measurement uncertainty (in mÅ). The tabulated widths are the *measured* line widths: we have not removed the instrumental profile. This provides the reader with a bit more information on the very narrow lines than just giving an upper limit on the width. The instrumental width can be removed by using the simple relation among the intrinsic, measured, and instrumental widths: $\text{FWHM}_{\text{intrinsic}}^2 = \text{FWHM}_{\text{measured}}^2 - \text{FWHM}_{\text{instrumental}}^2$. The intensity of the Fe ix line at 171.074 Å is given in parentheses because this line lies outside the range within which the calibration curve was derived. Tentative line identifications are also given in parentheses. Because the majority of the lines in Table 2 orig-

inate in the seven successive ionization stages of iron between x and xvi and because we have relied heavily upon those lines to derive the SERTS-95 relative radiometric calibration, we discuss the emission lines from each of these ionization stages in separate subsections below.

Fe x, xi, xii, xiii, and xiv each contain several line intensity ratios that are sensitive to electron density. Larger variations in theoretical ratios correspond to smaller uncertainties in derived electron densities; small variations in theoretical ratios can yield essentially undetermined electron densities. In the following subsections we use ratios which vary by factors of 10 or more over a range of typical coronal densities ($8.5 \leq n_e \leq 10.5$) in order to minimize measurement uncertainties on derived densities. Mason et al. (1997) present preliminary results of electron density diagnostics using the *SOHO/CDS*.

4.1. Fe x

We observed seven Fe x lines, at wavelengths of 174.526, 175.265, 177.240, 184.534, 190.046, 220.862, and 257.246 Å. Four of these (174.526, 177.240, 184.534, and 190.046) comprise a density-insensitive combination that was used for calibration of the second order wave band (see Table 3), while another (175.265) provides an excellent density diagnostic when taken as a ratio with any of the first four. From Table 2 we obtain an intensity ratio of 0.206 ± 0.056 for 175.265/174.526; a cubic spline interpolation on the corresponding CHIANTI density sensitivity curve yields an Fe x logarithmic electron density of $9.40^{+0.20}_{-0.25}$.

Based upon intensity ratios involving the Fe x lines at 220.862 and 257.246 Å, these two lines are too intense by factors ~ 9 and ~ 13 , respectively. The discrepancy between theory and observation for the 220.862 line may be due to blending with a relatively strong line at similar wavelength from an undetermined ionization stage of iron (Kelly 1987), which does not appear in the CHIANTI data. Similarly, the discrepancy for the 257.246 line may be due to blending with a Si ix line at 257.255 Å (Kelly 1987), which is not included in CHIANTI.

4.2. Fe xi

We observed eleven Fe xi lines, at wavelengths of 180.382, 181.125, 182.166, 184.800, 188.214, 188.295, 189.185, 189.722, 192.813, 222.998, and 308.545 Å. Three of these comprise one density-insensitive group (181.125, 182.166, and 189.722), while two others comprise a second such group (188.214 and 192.813). See Table 3. Although the strongest Fe xi line (180.382) should also be a member of the second density-insensitive group, it is blended with the strong first-order Fe xvi resonance line at 360.76 Å (for which the relative intensity is not reliably calibrated) and is therefore not useful for active region diagnostics. (It is, however, useful in the quiet-Sun spectrum, in which Fe xvi emission is negligible).

We tentatively associate the 188.295 line with Fe xi (its identification is given in parentheses in Table 2), noting that Kelly (1987) does not include this relatively strong line in his Finding List and that Dere (1978) does not report this line in solar flare spectra. CHIANTI indicates that this line should be a member of the second density-insensitive group above and that the 188.295/188.214 intensity ratio should be 0.380 ± 0.016 . We find the ratio to be 0.718 ± 0.196 from our active region spectrum, while the Behring et al. (1976) full-Sun spectrum yields a ratio of 0.70. (Note that the uncertain relative radiometric calibration of the Behring et al. observations does not affect the intensity ratio of these closely spaced lines.) The Kelly (1987) list includes a Si line (from an undetermined ionization stage) at 188.3 Å. We also tentatively associate the 189.185 line with Fe xi, noting that although this line's intensity relative to that of Fe xi 189.719 (1.24 ± 0.46) matches the theoretical branching ratio (1.30), the measured wavelength is higher than expected (189.129 Å). Kelly (1987) indicates a Mn ix line at 189.16 Å and a Ni xv line at 189.21 Å. The weak line at 222.998 Å, near the end of both the second-order wave band and the film itself, is likely a blend of Fe xi and Ca xvii; its measured intensity is more than 10 times greater than theoretically predicted for the lines in the second group above.

Intensity ratios among the lines in the two different density-insensitive groups above form density-sensitive ratios. These ratios vary only by factors $\lesssim 4$ for $8.5 \leq \log n_e \leq 10.5$, so they provide relatively uncertain density measurements. However, ratios of the 184.800 line to the strongest line in each group above yield variations by factors of 15 and 37, respectively, so these ratios provide good measures of the electron density in the Fe xi-emitting region. The measured intensity ratio of 184.800/182.166 is 0.133 ± 0.062 , which yields $\log n_e = 9.33^{+0.27}_{-0.41}$; the measured 184.800/188.214 ratio is 0.0818 ± 0.0399 , which yields $\log n_e = 9.54^{+0.21}_{-0.33}$. Both of these values agree (within the measurement uncertainty) with the density derived for Fe x. The 308.545 line appears to be blended with an Fe vi line at 308.539 Å (Kelly 1987).

4.3. Fe xii

We observed nine Fe xii lines, at wavelengths of 186.867, 192.390, 193.505, 195.117, 196.642, 211.736, 214.400, 217.277, and 219.449 Å. The lines at 186.867 and 195.117 are self-blends of lines at 186.851 and 186.884 Å and at 195.118 and 195.131 Å; contributions from both components of each line were incorporated in all theoretical ratios involving those lines. The 186.867, 196.642, and 219.449 lines are members of one density-insensitive line group, and the 192.390, 193.505, 195.117, and 211.736 lines are members of another. See Table 3.

The line at 217.277 Å belongs in the first density-insensitive group above, but its observed intensity is a factor ~ 3 too high; the measured ratio of 1.31 ± 0.63 for the 217.277/219.449 intensities is significantly greater than the corresponding theoretical branching ratio of 0.414. The only viable candidate for possible blending (Kelly 1987) belongs to Fe xxii. (We see a hint, but not a reliable detection, of only the strongest Fe xxii line, at 247.143 Å.) The line at 214.400 Å belongs in the second density-insensitive group above, but its intensity relative to those lines is a factor ~ 6 too high. No good blending candidates are found in Kelly (1987). It is possible that the theoretical intensities for both the 217.277 and 214.400 lines need revision.

Theoretical intensity ratios between lines from the first and second Fe xii density-insensitive groups vary by factors ~ 7 for $8.5 \leq \log n_e \leq 10.5$. The 186.867/195.117 ratio of 0.573 ± 0.099 yields an electron density of $10.08^{+0.21}_{-0.23}$, while the 196.642/193.505 ratio of 0.247 ± 0.046 yields an electron density of $10.00^{+0.20}_{-0.24}$. These values are significantly greater than the densities derived from ratios of lines from other ions in this active region. Brosius et al. (1996a) found comparably high densities from Fe xii 338.3/352.1 in active region, quiet-Sun, and off-limb spectra from three previous SERTS flights.

4.4. Fe xiii

We observed nineteen Fe xiii lines, at wavelengths of 196.519, 200.017, 201.118, 202.042, 202.415, 203.164, 203.820, 204.255, 204.950, 209.623, 209.908, 213.764, 221.813, 240.687, 246.187, 251.939, 312.167, 318.100, and 320.796 Å. These provide four different density-insensitive line groups, the first of which is comprised of seven lines (200.017, 203.164, 203.820, 204.255, 209.623, 221.813, and 320.796), the second of which is comprised of two (202.042 and 209.908), the third of which is comprised of two (201.118 and 204.950), and the fourth of which is comprised of three (240.687, 246.187, and 251.939). See Table 3. The line at 203.820 Å is a self-blend of lines at 203.797 and 203.828 Å. Contributions from both components are incorporated in all theoretical ratios involving this line.

We associate the line at 202.415 Å with Fe xiii rather than with Fe xi (as suggested by CHIANTI) for two reasons. First, the Kelly (1987) Finding List includes an Fe xiii line at 202.424 Å, but it does not include an Fe xi line at any comparable wavelength. Second, if we assume the line to be associated with Fe xi, we obtain from CHIANTI a density-insensitive ratio of 0.054 relative to the Fe xi line at 188.214 Å but find that the corresponding observed value (0.191 ± 0.059) is a factor ~ 4 too high.

The theoretical branching ratio of the 213.771 line to the 209.621 line is nearly unity, but the observed value (0.438 ± 0.120) is only about half the expected value. This discrepancy cannot be due to blending of the 209.621 line,

since that line forms excellent density-insensitive ratios with six other Fe xiii lines. The SERTS-89 active region spectrum (Thomas & Neupert 1994) yielded a similarly low ratio, although the measurement uncertainty in those observations is considerably greater than it is here (Young et al. 1998). This discrepancy remains to be resolved.

The electron density of the Fe xiii-emitting plasma can be measured by taking intensity ratios between lines from different density-insensitive groups above, as well as by taking ratios with other available lines. The 209.623/209.908 intensity ratio provides an excellent density diagnostic not only because the lines are so closely spaced that uncertainties in any relative radiometric calibration are negligible but also because the theoretical ratio varies by a factor ~ 18 between $\log n_e = 8.5$ and $\log n_e = 10.5$. The measured ratio of 0.932 ± 0.233 yields a logarithmic electron density of $9.37^{+0.14}_{-0.16}$. Similarly, the 203.820/202.042 ratio provides a measured value of 1.59 ± 0.27 , which yields a logarithmic density of $9.55^{+0.11}_{-0.12}$. The 196.519/202.042 ratio varies by a factor of 110 for $8.5 \leq \log n_e \leq 10.5$, and the corresponding measured ratio of 0.111 ± 0.030 yields a logarithmic density of $9.38^{+0.08}_{-0.11}$. All of these densities are consistent with those derived from Fe x and Fe xi above. Several of the ratios yield somewhat higher values (e.g., 196.519/251.939 yields $\log n_e = 9.71^{+0.18}_{-0.23}$, and 318.100/312.167 yields $\log n_e = 9.68^{+0.21}_{-0.30}$), while others yield somewhat lower values (e.g., 196.519/201.118 yields $\log n_e = 9.19^{+0.16}_{-0.22}$, and 196.519/312.167 yields $\log n_e = 9.09^{+0.12}_{-0.16}$).

4.5. Fe xiv

We observed 10 Fe xiv lines, at wavelengths of 211.317, 219.121, 220.090, 252.168, 257.370, 264.768, 270.511, 274.193, 289.140, and 334.167 Å. Except where noted, our analysis of the Fe xiv line intensity ratios is based upon recent computations performed and kindly provided by P. J. Storey (1998, private communication). The 252.168 and 264.768 lines are members of one density-insensitive line group, while the 211.317, 220.090, 274.193, 289.140, and 334.167 lines are members of a second. See Table 3.

Intensity ratios between lines in the first density-insensitive group and lines in the second are density sensitive; however, they vary by factors of only ~ 3.5 and so are not ideal for accurately measuring densities. Our observed 264.768/274.193 ratio of 0.933 ± 0.167 is consistent with the corresponding theoretical range of 1.55 ± 0.87 . The 219.121/211.317 intensity ratio varies by a factor ~ 13 between $8.5 \leq \log n_e \leq 10.5$, and our observed value of

0.298 ± 0.049 yields an electron density of 9.26 ± 0.10 . The corresponding density derived from CHIANTI version 1.01 is $9.38^{+0.09}_{-0.10}$, in good agreement with the value derived with the recent calculations of P. J. Storey (1998, private communication). Further, these densities are consistent with the values derived from Fe x, xi, and xiii above.

The recent calculations of P. J. Storey (1998, private communication) appear to resolve an old discrepancy between the theoretical and observed values of the 270.511/274.193 ratio. The CHIANTI package yields a ratio of 1.241 ± 0.077 , while corresponding observed values are 0.497 ± 0.108 (this work), 0.475 ± 0.083 (Thomas & Neupert 1994), and ~ 0.64 (Behring et al. 1976). The Storey calculations reveal the ratio to be slightly density sensitive, varying from ~ 0.4 at low densities to ~ 1 at high. Although the observed intensity ratio of 257.370/211.317 (0.118 ± 0.041) is about one-half the theoretically predicted value (0.247 ± 0.067), the uncertainties are large enough that this difference is only marginally significant.

4.6. Fe xv

We observed two Fe xv lines, at wavelengths of 243.771 and 284.151 Å. These lines comprise a density-insensitive group, as shown in Table 3. No density-sensitive ratios were observed for this ion.

4.7. Fe xvi

We observed three Fe xvi lines, at wavelengths of 251.053, 262.965, and 335.401 Å. All of these are members of the density-insensitive group seen in Table 3. No density-sensitive ratios are available for this ion.

5. QUIET-SUN SPECTRUM

A list of the emission lines observed in quiet-Sun areas northeast of NOAA region 7870 is given in Table 1. The list includes 19 second-order lines and only one first-order line (He ii $\lambda 303.782$). Table 1 is organized in the same way as Table 2. Note that while the hottest ion detected in the active region is Ca xvii ($\log T_{\max} = 6.69$), the hottest ion detected in the quiet Sun is Fe xiii ($\log T_{\max} = 6.20$). Table 4 is organized in the same way as Table 3 and lists the density- and temperature-insensitive line groups available in the quiet-Sun spectrum. Column (5) gives the ratio of observed to theoretical intensities, normalized by the weighted average ratio within each group. Here all nine of

TABLE 4
SERTS-95 INSENSITIVE RATIOS FROM QUIET SUN

Ion (1)	Wavelength (2)	Normalized Theoretical I (3)	Normalized Observed I (4)	Normalized Observed/ Theoretical (5)
Fe x	174.534	1.0000 ± 0.0000	1.0000 ± 0.1976	1.0592 ± 0.2093
	177.246	0.6190 ± 0.0140	0.4551 ± 0.1503	0.7787 ± 0.2577
	184.548	0.2560 ± 0.0100	0.3274 ± 0.1015	1.3547 ± 0.4232
Fe xi	180.405	1.0000 ± 0.0000	1.0000 ± 0.1451	1.0766 ± 0.1562
	188.218	0.4990 ± 0.0300	0.3786 ± 0.1030	0.8169 ± 0.2276
	192.827	0.1040 ± 0.0060	0.1005 ± 0.0304	1.0408 ± 0.3207
Fe xii	192.385	0.2120 ± 0.0020	0.3182 ± 0.0813	1.4090 ± 0.3604
	193.512	0.5540 ± 0.0440	0.6286 ± 0.1199	1.0650 ± 0.2200
	195.128	1.0000 ± 0.0000	1.0000 ± 0.1245	0.9386 ± 0.1169

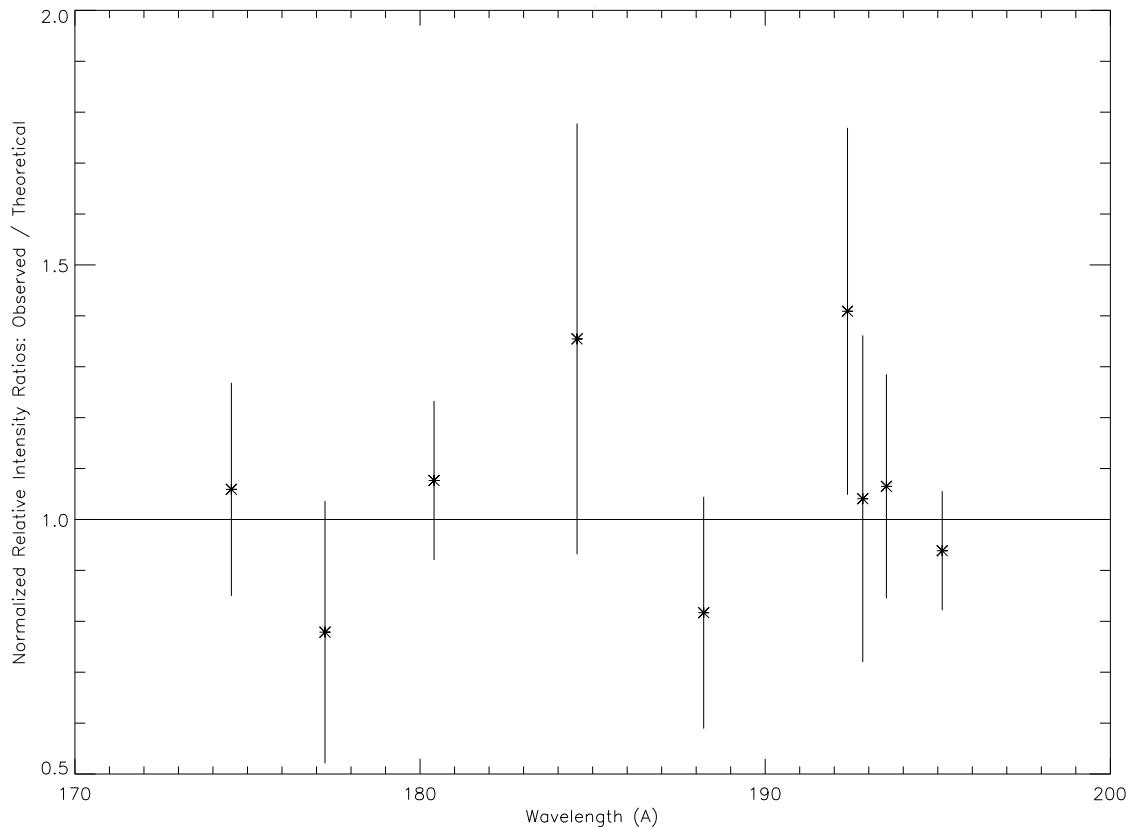


FIG. 4.—Same as Fig. 2, but for the quiet Sun (Table 4)

the available ratios are unity within (or nearly within) their 1σ measurement uncertainties. This is illustrated in Figure 4, in which we plot the values in column (5) as a function of wavelength. The quiet-Sun insensitive ratios are in excellent agreement with their active region counterparts.

5.1. Fe x

We observed three Fe x lines, at wavelengths of 174.534, 177.246, and 184.548 Å. All of these lines are members of a density-insensitive group, as shown in Table 4. No density-sensitive ratios are available for this ion in the quiet-Sun spectrum.

5.2. Fe xi

We observed five Fe xi lines, at wavelengths of 180.405, 182.157, 188.218, 188.303, and 192.827 Å. Three of these lines (180.405, 188.218, and 192.827) are members of a density-insensitive line group, as shown in Table 4. As in the active region spectrum above, we tentatively associate the 188.303 line with Fe xi; however, also as in the active region spectrum we note that the 188.303/188.218 intensity ratio of 0.689 ± 0.233 is significantly greater than the theoretical value of 0.380 ± 0.016 . Intensity ratios between the 182.157 line and lines in the density-insensitive group are only slightly density sensitive; therefore, we do not report density measurements for this ion.

5.3. Fe xii

We observed four Fe xii lines, at wavelengths of 186.885, 192.385, 193.512, and 195.128 Å. A fifth line, at 201.733 Å,

was identified as Fe xii by Behring et al. (1976), Dere (1978), and Feldman, Purcell, & Dohne (1987) but is unidentified in CHIANTI (Dere et al. 1997); Kelly (1987) lists no Fe xii line at this wavelength but has an Fe xi line at 201.737. This line is observed at 201.759 Å in the active region spectrum. Three of the Fe xii lines (192.385, 193.512, and 195.128) are members of a density-insensitive group and are listed in Table 4. The ratio of the 186.885 line to any of the lines in the density-insensitive group provides a measurement of the electron density. The 186.885/195.128 ratio of 0.237 ± 0.092 yields a logarithmic electron density of $9.14^{+0.33}_{-0.45}$.

5.4. Fe xiii

We observed two Fe xiii lines, at wavelengths of 202.056 and 203.836 Å. The 203.836/202.056 ratio is density sensitive, and its measured value of 0.366 ± 0.141 yields a logarithmic density of $8.81^{+0.14}_{-0.21}$. This density is ~ 0.18 the active region density derived from the same line ratio and is consistent (within the measurement uncertainties) with the density derived from Fe xii above.

J. W. B. acknowledges NASA support through contract NASW-96006. J. M. D. and R. J. T. acknowledge NASA support for the SERTS program by RTOP grants from the Solar Physics Office of NASA's Space Physics Division. We acknowledge valuable discussions with W. E. Behring, E. Landi, and P. R. Young. We thank P. J. Storey for providing us with results from his Fe xiv calculations prior to their publication and the anonymous referee for providing suggestions that helped improve the manuscript.

REFERENCES

- Arnaud, M., & Raymond, J. 1992, *ApJ*, 398, 394
- Arnaud, M., & Rothenflug, R. 1985, *A&AS*, 60, 425
- Behring, W. E., Cohen, L., Feldman, U., & Doschek, G. A. 1976, *ApJ*, 203, 521
- Brosius, J. W., et al. 1993, *ApJ*, 411, 410
- Brosius, J. W., Davila, J. M., & Thomas, R. J. 1998, *ApJ*, 497, L113
- Brosius, J. W., Davila, J. M., Thomas, R. J., & Monsignori-Fossi, B. C. 1996a, *ApJS*, 106, 143
- Brosius, J. W., Davila, J. M., Thomas, R. J., Monsignori-Fossi, B. C., & Jordan, S. D. 1996b, in *UV and X-Ray Spectroscopy of Astrophysical and Laboratory Plasmas*, ed. K. Yamashita & T. Watanabe (Tokyo: Universal Academy), 83
- Brosius, J. W., Davila, J. M., Thomas, R. J., Saba, J. L. R., Hara, H., & Monsignori-Fossi, B. C. 1997a, *ApJ*, 477, 969
- Brosius, J. W., Davila, J. M., Thomas, R. J., & White, S. M. 1997b, *ApJ*, 488, 488
- Chapman, R. D., & Neupert, W. M. 1974, *J. Geophys. Res.*, 79, 4138
- Davila, J. M., Thomas, R. J., Thompson, W. T., Keski-Kuha, R. A. M., & Neupert, W. M. 1993, in *UV and X-Ray Spectroscopy of Astrophysical and Laboratory Plasmas*, ed. E. Silver & S. Kahn (Cambridge: Cambridge Univ. Press), 301
- Dere, K. P. 1978, *ApJ*, 221, 1062
- Dere, K. P., Landi, E., Mason, H. E., Monsignori-Fossi, B. C., & Young, P. R. 1997, *A&AS*, 125, 149 (CHIANTI, version 1.01)
- Dere, K. P., Mason, H. E., Widing, K. G., & Bhatia, A. K. 1979, *ApJS*, 40, 341
- Doschek, G. A., & Cowan, R. D. 1984, *ApJS*, 56, 67
- Feldman, U., Purcell, J. D., & Dohne, B. C. 1987, *An Atlas of Extreme Ultraviolet Spectroheliograms from 170 to 625 Å* (NRL Reports 90-4100 and 91-4100) (Washington: NRL)
- Heroux, L., Cohen, M., & Higgins, J. E. 1974, *J. Geophys. Res.*, 79, 5237
- Higgins, J. E. 1976, *J. Geophys. Res.*, 81, 1301
- Kelly, R. L. 1987, *J. Phys. Chem. Ref. Data*, 16, Suppl. 1 (Finding List)
- Landi, E., Del Zanna, G., Landini, M., Bromage, B. J. I., Breeveld, E. R., & Pike, C. D. 1998a, in preparation
- Landi, E., Landini, M., Pike, C. D., & Mason, H. E. 1998b, *Sol. Phys.*, in press
- Linsky, J. L., Glackin, D. L., Chapman, R. D., Neupert, W. M., & Thomas, R. J. 1976, *ApJ*, 203, 509
- Malinovsky, M., & Heroux, L. 1973, *ApJ*, 181, 1009
- Mango, S. A., Bohlin, J. D., Glackin, D. L., & Linsky, J. L. 1978, *ApJ*, 220, 683
- Mason, H. E., Young, P. R., Pike, C. D., Harrison, R. A., Fludra, A., Bromage, B. J. I., & Del Zanna, G. 1997, *Sol. Phys.*, 170, 143
- Neupert, W. M., Epstein, G. L., Thomas, R. J., & Thompson, W. T. 1992, *Sol. Phys.*, 137, 87
- Neupert, W. M., & Kastner, S. O. 1983, *A&A*, 128, 188
- Ogawa, H. S., Judge, D. L., McMullin, D. R., Gangopadhyay, P., & Galvin, A. B. 1998, *J. Geophys. Res.*, 103, 1
- Thomas, R. J., & Neupert, W. M. 1994, *ApJS*, 91, 461
- Thompson, W. T., Neupert, W. M., Jordan, S. D., Jones, H. P., Thomas, R. J., & Schmieder, B. 1993, *Sol. Phys.*, 147, 29
- Timothy, A. F., & Timothy, J. G. 1970, *J. Geophys. Res.*, 75, 6950
- Tousey, R., Bartoe, J.-D. F., Brueckner, G. E., & Purcell, J. D. 1977, *Appl. Opt.*, 16, 870
- Vernazza, J. E., & Reeves, E. M. 1978, *ApJS*, 37, 485
- Woods, T. N., Rottman, G. J., Bailey, S. M., Solomon, S. C., & Worden, J. R. 1998, *Sol. Phys.*, 177, 133
- Young, P. R., Landi, E., & Thomas, R. J. 1998, *A&A*, 329, 291